Notes on Fault Slip Analysis

Prepared for the Geological Society of America Short Course on

"Quantitative Interpretation of Joints and Faults"

November 4 & 5, 1989

by

Richard W. Allmendinger

with contributions by

John W. Gephart & Randall A. Marrett

Department of Geological Sciences
Cornell University Ithaca, New York
14853-1504

TABLE OF CONTENTS

PREFACE

Structural geology has, classically, been more concerned with the study of ductile deformation. Homogeneous deformation of a fossil conveniently lends itself to the application of continuum mechanics principles. Faults, on the other hand, are discrete discontinuities in the rock and thus their analysis is much more complicated. It is, perhaps, a measure of where we stand in faulting analysis that the work of Amontons (1699) and Coulomb (1773) still comprise the most widely used approaches to the problem.

In the last decade, with the heightened interest in neotectonics and active mountain building processes, there has been an explosion in the number of quantitative analyses of fault data sets. In an active mountain belt, the ductile deformation remains hidden at depth and faults constitute one of the few geological features available for structural study.

The present methods of faulting analysis fall into two groups: kinematic and dynamic. In addition, in each general class, one can analyze the data with either numeric or graphical methods. These notes begin by giving some of the theoretical background behind numerical methods of both dynamic and kinematic methods (sections 1 and 2). Two of the most robust graphical methods are presented in section 3; no attempt is made in that section to cover all of the graphical methods proposed by various authors, although the appropriate references are given. Section 4 on “practical applications” presents some of the most important aspects of faulting analysis for the field geologist. Not only are sense of shear indicators reviewed, but features possibly indicative of scale invariance of the faulting process are described. The fractal distribution of faults and fault-related features is among the most exciting new topics in structural geology and geophysics. Finally, section 4 ends with some guidelines for interpreting heterogeneous data. The temptation is to interpret all heterogeneous data as the result of multiple deformations, but there are several other processes which can also produce such results.

The application of these faulting analysis methods is relatively easy due to the proliferation of powerful microcomputers. However, we caution against the blind application of the techniques presented here without full realization of the assumptions involved and without the complete evaluation of the appropriateness of the methods. The old adage, “garbage in, garbage out,” clearly applies here, regardless of how good the statistics look. Finally, we cannot emphasize strongly enough the necessity of complete field work in the region of study. In particular, the establishment of relative and absolute age relations is of critical importance. The field relations contain the ultimate clues to, and the ultimate justification for, application of these methods.

1. STRESS FROM FAULT POPULATIONS

by J. W. Gephart and R. W. Allmendinger

1.1 -- INTRODUCTION

Since the pioneering work of Bott (1959), many different methods for inferring certain elements of the stress tensor from populations of faults have been proposed. These can be grouped in two broad categories: graphical methods (Compton, 1966; Arthaud, 1969; Angelier and Mechler, 1977; Aleksandrowski, 1985; and Lisle, 1987) and numerical techniques (Carey and Brunier, 1974; Etchecopar et al., 1981; Armijo et al., 1982; Angelier, 1984, 1989; Gephart and Forsyth, 1984; Michael, 1984; Reches, 1987; Gephart, 1988; Huang, 1988). In this section, we review the theoretical basis for the numerical stress inversion methods, following the analysis of Gephart and Forsyth (1984) and Gephart (in review). Practical application, as well as graphical methods, are discussed in a subsequent section.

1.2 -- ASSUMPTIONS

Virtually all numerical stress inversion procedures have the same basic assumptions:

1. Slip on a fault plane occurs in the direction of resolved shear stress (implying that local heterogeneities that might inhibit the free slip of each fault plane -- including interactions with other fault planes -- are relatively insignificant).

2. The data reflect a uniform stress field (both spatially and temporally)—this requires that there has been no post-slip deformation of the region which would alter the fault orientations.

While the inverse techniques may be applied to either fault/slickenside or earthquake focal mechanism data, both of which indicate the direction of slip on known fault planes (neglecting for now the ambiguity of nodal planes in focal mechanisms), these assumptions may apply more accurately to the latter than the former. Earthquakes may be grouped in geologically short time windows, and represent sufficiently small strains that rotations may be neglected. Faults observed in outcrop, on the other hand, almost certainly record a range of stresses which evolved through time, possibly indicating multiple deformations. If heterogeneous stresses are suspected, a fault data set can easily be segregated into subsets, each to be tested independently. In any case, to date there have been many applications of stress inversion methods

from a wide variety of tectonic settings which have produced consistent and interpretable results.

1.3 -- COORDINATE SYSTEMS & GEOMETRIC BASIS

Several different coordinate systems are use by different workers. The ones used here are those of Gephart and Forsyth (1984), with an unprimed coordinate system which is parallel to the principal stress directions, and a primed coordinate system fixed to each fault, with axes parallel to the pole, the striae, and the B-axis (a line in the plane of the fault which is perpendicular to the striae) of the fault, as shown below:

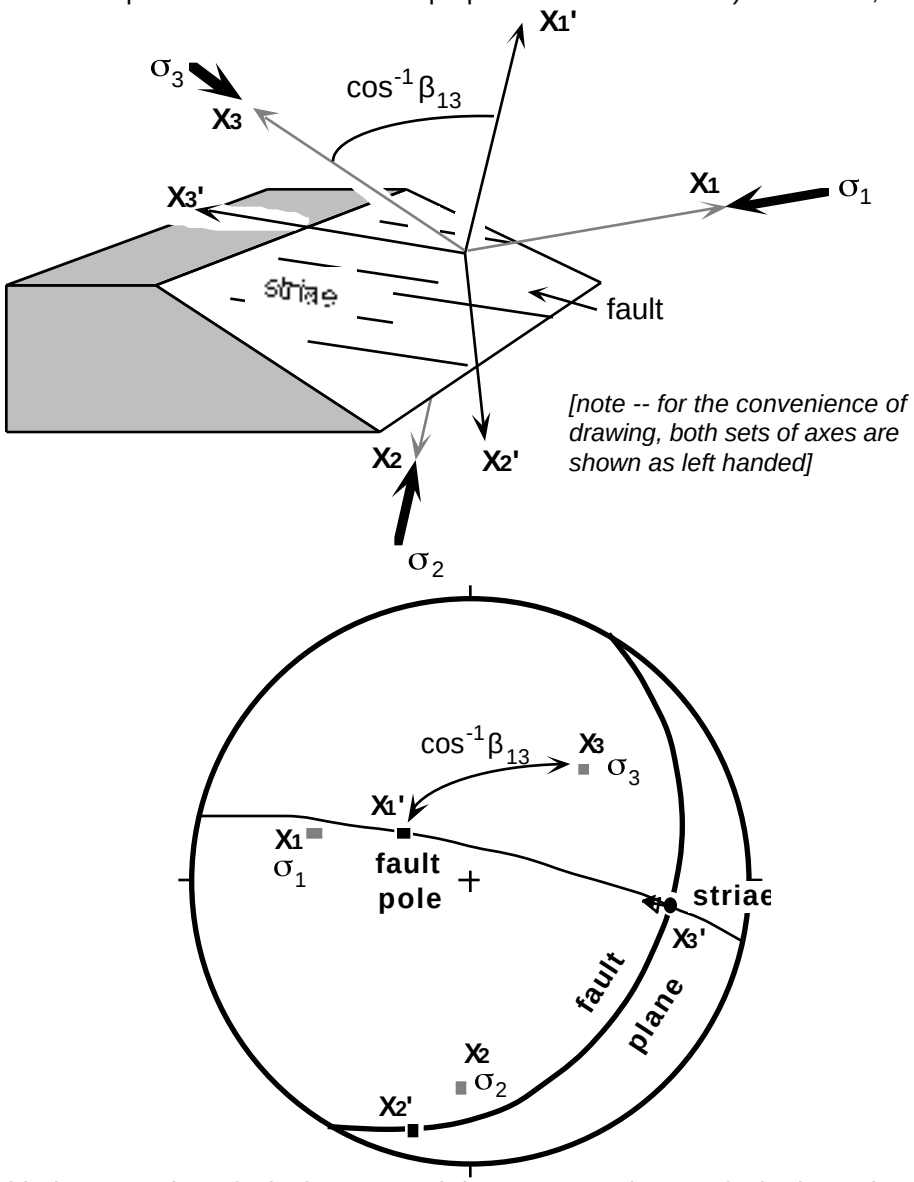

The relationship between the principal stress and the stress on the one fault plane shown is given by a standard tensor transformation:

$$\sigma_{ij}' = \beta_{ik}\,\beta_{jl}\,\sigma_{kl}\,.$$

In the above equation, β_{ik} is the transformation matrix reviewed earlier, σ_{kl} are the regional stress magnitudes, and σ_{ij}**'** are the stresses on the plane. Expanding the above equation to get the components of stress on the plane in terms of the principal stresses, we get:

$$\sigma_{11}' = \beta_{11}\beta_{11}\sigma_1 + \beta_{12}\beta_{12}\sigma_2 + \beta_{13}\beta_{13}\sigma_3 \qquad \text{[normal traction],}$$

$$\sigma_{12}' = \beta_{11}\beta_{21}\sigma_1 + \beta_{12}\beta_{22}\sigma_2 + \beta_{13}\beta_{23}\sigma_3 \qquad \text{[shear traction striae],}$$

and

$$\sigma_{13}' = \beta_{11}\beta_{31}\sigma_1 + \beta_{12}\beta_{32}\sigma_2 + \beta_{13}\beta_{33}\sigma_3 \qquad \text{[shear traction // striae].}$$

From assumption #1 above we require that σ_{12}**'** vanishes, such that:

$$0 = \beta_{11}\beta_{21}\sigma_1 + \beta_{12}\beta_{22}\sigma_2 + \beta_{13}\beta_{23}\sigma_3\,.$$

Combining this expression with the condition of orthogonality of the fault pole and B axis:

$$0 = \beta_{11}\beta_{21} + \beta_{12}\beta_{22} + \beta_{13}\beta_{23}\,.$$

yields

$$\frac{\sigma_2 - \sigma_1}{\sigma_3 - \sigma_1} \equiv R = -\frac{\beta_{13}\,\beta_{23}}{\beta_{12}\,\beta_{22}}\,. \qquad (1.3.1)$$

where the left-hand side defines the parameter, R, which varies between 0 and 1 (assuming that $\sigma_1 \geq \sigma_2 \geq \sigma_3$) and provides a measure of the magnitude of σ_2 relative to σ_1 and σ_3. A value of R near 0 indicates that σ_2 is nearly equal to σ_1; a value near 1 means σ_2 is nearly equal to σ_3[1]. Any combination of principal stress and fault orientations which produces R > 1 or R < 0 from the right-hand side of (1.3.1) is incompatible (Gephart, 1985). A further constraint is provided by the fact that the shear traction vector, σ_{13}', must have the same direction as the slip vector (sense of slip) for the fault; this is ensured by requiring that $\sigma_{13}' > 0$.

[1]An equivalent parameter was devised independently by Angelier and coworkers (Angelier et al., 1982; Angelier, 1984, 1989):

$$\Phi = \frac{\sigma_2 - \sigma_3}{\sigma_1 - \sigma_3}\,.$$

In this case, if $\Phi = 0$, then $\sigma_2 = \sigma_3$, and if $\Phi = 1$, then $\sigma_2 = \sigma_1$. Thus, $\Phi = 1 - R$.

Equation (1.3.1) shows that, of the 6 independent components of the stress tensor, only four can be determined from this analysis. These are the stress magnitude parameter, R, and three stress orientations indicated by the four β_{ij} terms (of which only three are independent because of the orthogonality relations).

1.4 -- INVERSION OF FAULT DATA FOR STRESS

Several workers have independently developed schemes for inverting fault slip data to obtain stresses, based on the above conditions but following somewhat different formulations. In all cases, the goal is to find the stress model (three stress directions and a value of R) which minimizes the differences between the observed and predicted slip directions on a set of fault planes.

1.4.1 -- Description of Misfit

The first task is to decide: What parameter is the appropriate one to minimize in finding the optimum model? The magnitude of misfit between a model and fault slip datum reflects either: (1) the minimum observational error, or (2) the minimum degree of heterogeneity in stress orientations, in order to attain perfect consistency between model and observation. Two simple choices may be considered: Many workers (e.g. Carey and Brunier, 1974; Angelier, 1979, 1984) define the misfit as the angular difference between the observed and predicted slip vector measured in the fault plane (referred to as a "pole rotation" because the angle is a rotation angle about the pole to the fault plane). This implicitly assumes that the fault plane is perfectly known, such that the only ambiguity is in the orientation of the striae (right side of figure below). Such an assumption may be acceptable for fault data from outcrop for which it is commonly easier to measure the fault surface orientation than the orientation of the striae on the fault surface. Alternatively, one can find the smallest rotation of coupled fault plane and striae about *any* axis that results in a perfect fit between data and model (Gephart and Forsyth, 1984)—this represents the smallest possible deviation between an observed and predicted fault slip datum, and can be much smaller than the pole rotation, as shown in the left-hand figure below (from Gephart, in review). This "minimum rotation" is particularly useful for analyzing earthquake focal mechanism data for which there is generally similar uncertainties in fault plane and slip vector orientations.

An added complication in working with earthquake data in this application is that the fault plane must be distinguished from among the two nodal planes of the focal mechanism, as the choice of the fault plane influences the derived stress tensor. In this case, if the inversion is performed by a grid search (see below), the fault plane may be identified (tentatively), after testing each plane independently, as the one which yields the smaller of two calculated minimum rotations (Gephart and Forsyth, 1984). In a test of this

approach by Michael (1987) using artificial focal mechanisms constructed from observed fault planes, the selection of the fault plane was shown to be accurate in 89% of the cases in which there was a clear difference between the two planes. Other inverse methods, not based on a grid search, require the a priori selection of the fault plane from each focal mechanism, generally based on limited geologic information; as shown by Michael (1987), incorrect choices can distort the results. Angelier (1984) dealt with the ambiguity of nodal planes by including both planes in the inversion (recognizing that obviously only one is correct); this approach is strictly valid only if the stresses are axisymmetric (R = 0 or R = 1) and the B-axis is coplanar with the equal principal stresses (Gephart, 1985).

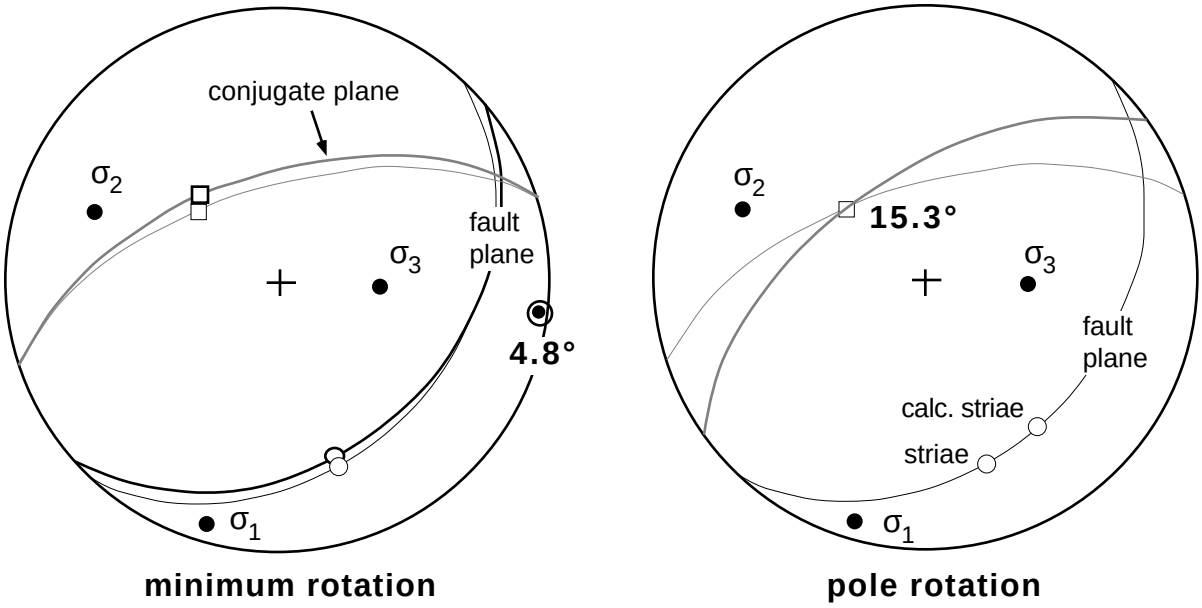

1.4.2 -- Identifying the Optimum Model

Because of the extreme non-linearity of this problem, the most reliable (but computationally demanding) procedure for finding the best stress model relative to a set of fault slip data involves the application of an exhaustive search of the four model parameters (three stress directions and a value of R) by exploring sequentially on a grid (Angelier, 1984; Gephart and Forsyth, 1984). For each stress model examined the rotation misfits for all faults are calculated and summed; this yields a measure of the acceptability of the model relative to the whole data set—the best model is the one with the smallest sum of misfits. Following Gephart and Forsyth (1984), confidence limits on the range of acceptable models can then be calculated using statistics for the one norm misfit, after Parker and McNutt (1980). In order to increase the computational efficiency of the inverse procedure, a few workers have applied some approximations which enable them

to linearize the non-linear conditions in this analysis (Angelier, 1984; Michael, 1984); naturally, these lead to approximate solutions which in some cases vary significantly from those of more careful analyses. The inversion methods of Angelier et al. (1982, eq. 9 p. 611) and Michael (1984) make the arbitrary assumption that the first invariant of stress is zero ($\sigma_{11} + \sigma_{22} + \sigma_{33} = 0$). Gephart (in review) has noted that this implicitly prescribes a fifth stress parameter, relating the magnitudes of normal and shear stresses (which should be mutually independent), the effect of which is seldom evaluated.

1.4.3 -- Normative Measure of Misfit

Following popular convention in inverse techniques, many workers (e.g. Michael, 1984; Angelier et al., 1982) have adopted least squares statistics in the stress inversion problem (e.g. minimizing the sum of the squares of the rotations). A least squares analysis, which is appropriate if the misfits are normally distributed, places a relatively large weight on extreme (poorly-fitting) data. If there are erratic data (with very large misfits), as empirically is often the case in fault slip analyses, then too much constraint is placed on these and they tend to dominate a least squares inversion. One can deal with this by rejecting anomalous data (Angelier, 1984, suggests truncating the data at a pole rotation of 45°), or by using a one-norm misfit, which minimizes the sum of the absolute values of misfits (rather than the squares of these), thus placing less emphasis on such erratic data, and achieving a more robust estimate of stresses (Gephart and Forsyth, 1984).

1.4.4 -- Mohr Circle and Mohr Sphere Constructions

The information derived in the stress inversion analysis can be displayed on an unscaled Mohr Circle, based on the stress magnitude parameter, R, and the principal stress orientations. [The construction of the three dimensional Mohr Circle for stress is reviewed by Jaeger and Cook, 2nd Ed., 1976, p. 27-30.] This is interesting because the stress inversion does not in any way regard the relative magnitudes of normal and shear stresses on the fault planes, and thus does not ensure that the stress models derived in the analysis are consistent with any reasonable failure criteria relative to the data. Thus, it is possible that acceptable stresses from this analysis could yield negligible shear stress or large normal stress on some fault planes—a condition that may be physically unreasonable but nonetheless satisfactory based on the present assumptions.

The figure below, from Gephart and Forsyth (1984), shows two alternative stress models for the San Fernando earthquake sequence; these represent local minima in the distribution of reasonable stresses. Model A has an average misfit of 8.1° and model B has an average misfit of 8.7°. Assuming that slip should occur selectively on planes that have relatively high shear stresses and low normal stresses, the model A

is preferred over model B because relative to the former the fault planes are concentrated in the upper and lower left parts of the diagram, while relative to the latter they are more widely scattered.

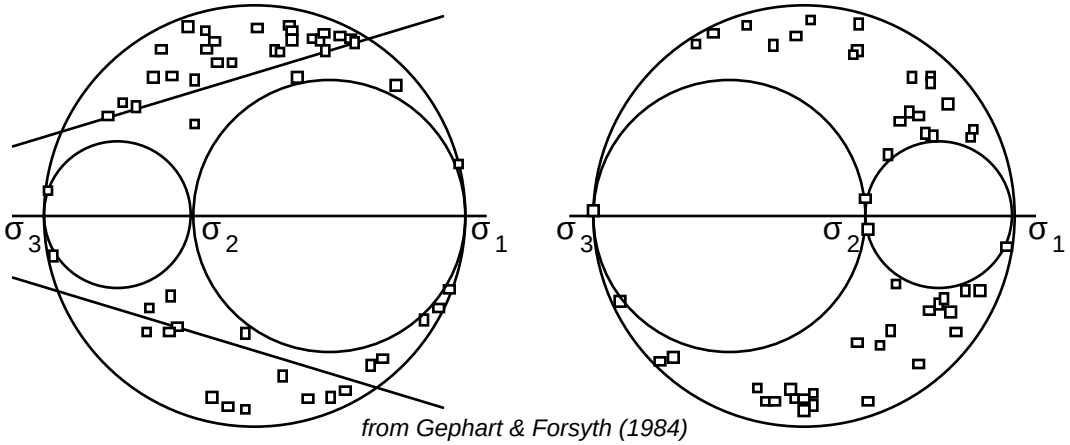

from Gephart & Forsyth (1984)

Model A:
R = 0.65
σ_1 = 187°, 07°
σ_2 = 281°, 27°
σ_3 = 084°, 62°

Model B:
R = 0.35
σ_1 = 170°, 00°
σ_2 = 260°, 09°
σ_3 = 080°, 81°

The Mohr Circle diagram considers only the magnitudes of shear and normal stress on any fault plane relative to a particular stress tensor. It may be expanded to consider the shear stress direction by considering two orthogonal components of shear stress; if these are plotted perpendicular to the Mohr Circle normal stress axis, the result is a spherical figure, referred to by Gephart (in review, 1989) as the Mohr Sphere construction (see figure below). This is useful for considering the relation between stress and fault slip data: Whereas in the Mohr Circle poles to all fault planes plot in the area between the largest and two smallest circles, in the Mohr Sphere all fault slip data plot as points in the volume between the largest and two smallest spheres. If the shear stress components are chosen along the kinematic axes (slip direction and B axis—τ_s and τ_b, respectively), then slip and shear stress directions are coincident if and only if the corresponding points plot on the [$\tau_b = 0$, $\tau_s > 0$] half-plane. Thus, the [$\tau_b = 0$, $\tau_s > 0$] half-plane is a graphical illustration of all solutions to equation (1.3.1). The object of the stress inversion procedure is to compare observed (non-fitting) fault slip data to acceptable (fitting) ones; the significance of various strategies for this can be illustrated using the Mohr Sphere diagram (Gephart, in review).

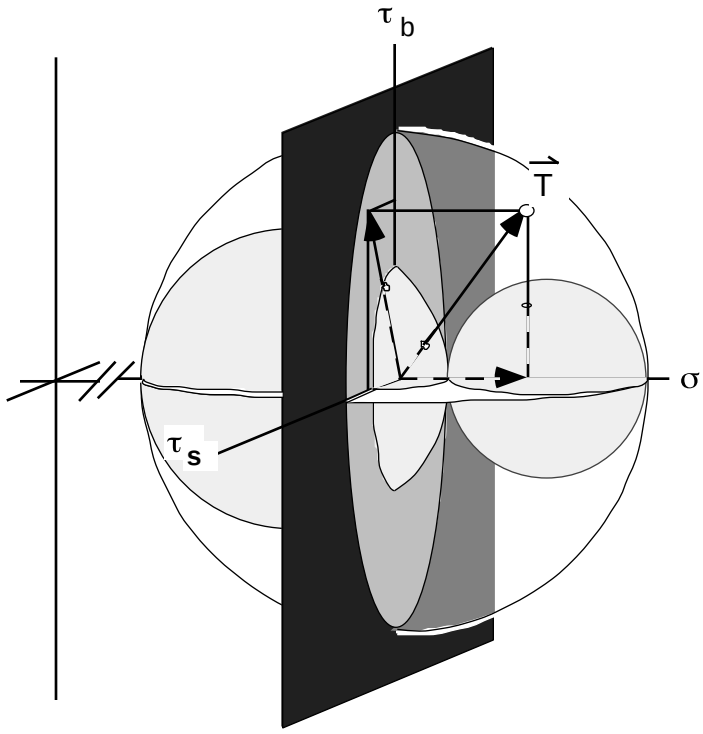

1.5 -- ESTIMATING AN ADDITIONAL STRESS PARAMETER

Up to this point we have considered efforts to infer four stress parameters from observations of slip directions on fault planes, based on the assumption that shear stress and slip directions are aligned. Additional information about the stress tensor may be inferred if we apply further assumptions on the relation between the stresses acting on fault planes. Several workers have explored this prospect by various approaches (Reches, 1987; Célérier, 1988; Gephart, 1988; Angelier, 1989). Here we introduce the formulation of Gephart (1988).

It is generally accepted, based on laboratory studies (Byerlee, 1978), that the magnitudes of shear and normal stress on sliding rock surfaces are linearly related, as most simply stated by Amonton's Law:

$$\tau = \mu\sigma_n ,$$

where μ is the coefficient of friction.

If we accept this condition, it is possible to estimate one additional number of the stress tensor (a fifth one, of the total of six), which relates the magnitudes of normal and shear stresses, either in reference to

specific fault planes (i.e. σ_{11}' and σ_{13}' in section (3)) or the general stress tensor, relating characteristic normal[2] and shear stresses, respectively:

$$\sigma_m \equiv \frac{\sigma_1 + \sigma_3}{2} \quad \text{and} \quad \tau_m \equiv \frac{\sigma_1 - \sigma_3}{2}$$

It is important to note that these numbers could not be related in the previous analysis of four stress parameters; it is only by applying an additional constraint that we can do this. The resulting stress tensor has one less degree of freedom than before, as illustrated below in the schematic profile of stress tensors with depth. In both cases, the Mohr Circles (defined by four parameters only) have the same shape at all depths. However, while in the four parameter case the sizes of the Mohr Circles are independent of normal stress (depth), in the five parameter case the size of the Mohr Circles must vary linearly with normal stress, according to Amonton's Law. Thus, the five parameter stress analysis applies much stronger constraints on the stress tensor, and may be much more difficult to satisfy than the four parameter analysis.

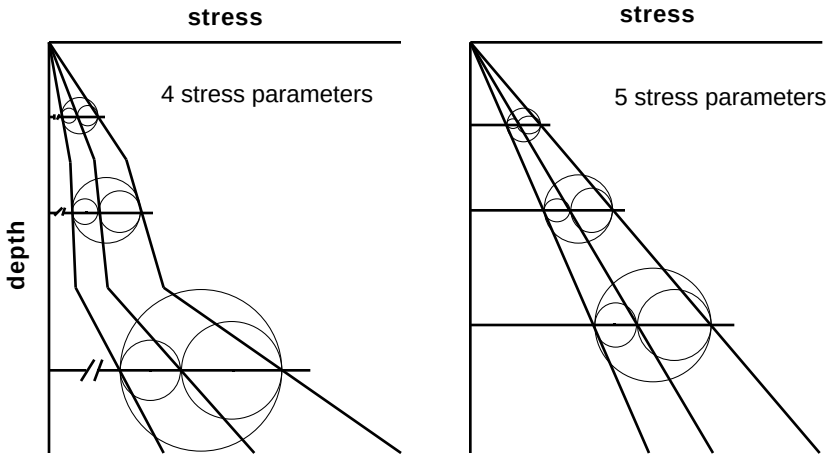

In order to optimize the five parameter stress tensor relative to a population of fault data, we must adopt an appropriate physical constraint which depends on the ratio of normal and shear stress on each fault plane. Gephart (1988) proposed that stresses be determined so as to optimize the fault orientations according to Amonton's Law; this is equivalent to minimizing the average deviatoric stress (minimizing the size of the Mohr Circle) required by the fault population.

[2]Note that σ_m as used here is neither the mean stress nor the maximum stress but the center of the Mohr's circle.

The last (sixth) number of the stress tensor fixes the scaling factor, and thus the magnitude of all stress elements. Because this number is scaled, it cannot be estimated from orientations, which are inherently dimensionless.

2. STRAIN FROM FAULTS: THE MOMENT TENSOR SUMMATION

by R. W. Allmendinger

2.1 -- GEOMETRY

Consider a block of material with a single fault in it (this derivation follows after Molnar, 1983):

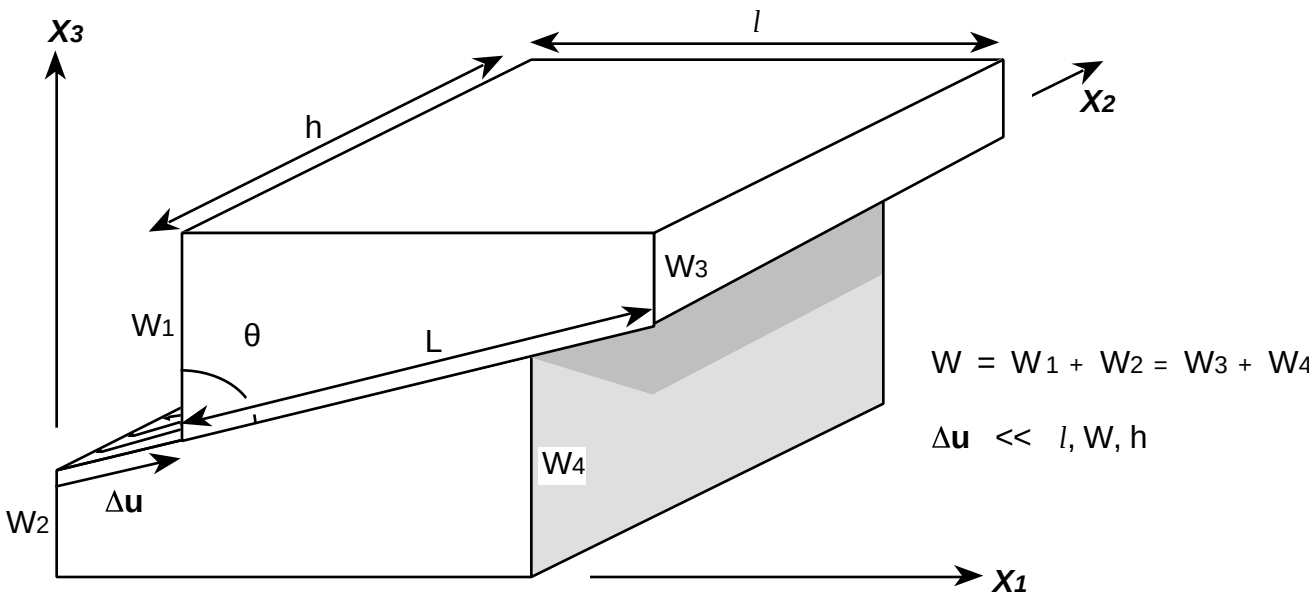

Because the slip, $\Delta\mathbf{u}$, is much smaller than the dimensions of the block, we can assume infinitesimal strain.

Before going into strain, however, we need to introduce the concept of **moment**. Seismologists commonly use a scalar parameter known as the seismic moment:

$$M_o = \mu \text{ (fault surface area) (average slip)},$$

where μ is the shear modulus. For the purposes of fault slip data analysis we can omit the shear modulus from the above equation and we are left with the **geometric moment**:

$$M_g = \text{(fault surface area) (average slip).}$$

Thus, for the block with the fault in it, above,

$$M_g = L\, h\, \Delta\mathbf{u}.$$

The *volume* of the region being deformed is:

$$V = l\, h\, W.$$

Solving for h and l, we get

$$h = \frac{V}{l\, W} \quad \text{and} \quad l = L \sin\theta.$$

So the geometric moment can be written:

$$M_g = L\left(\frac{V}{l\, W}\right)\Delta\mathbf{u} = L\left(\frac{V}{W\, L \sin\theta}\right)\Delta\mathbf{u} = \frac{V\, \Delta\mathbf{u}}{W \sin\theta}.$$

2.2 -- DERIVATION OF THE DISPLACEMENT GRADIENT TENSOR

Earlier on, we derived the displacement gradient tensor, e_{ij}:

$$\Delta u_i = e_{ij}\, \Delta X_j \qquad \text{where} \qquad e_{ij} = \frac{\partial u_i}{\partial X_j}.$$

Recall that e_{11} and e_{33} are just the extensions parallel to the axes of the coordinate system:

$$e_{11} = \frac{\Delta u_1}{\Delta X_1} \qquad \text{and} \qquad e_{33} = \frac{\Delta u_3}{\Delta X_3}$$

and that, because of our infinitesimal assumption, the off-diagonal components of the displacement gradient tensor are:

$$e_{13} = \frac{\Delta u_1}{\Delta X_3} \qquad \text{and} \qquad e_{31} = \frac{\Delta u_3}{\Delta X_1}.$$

Returning to our fault:

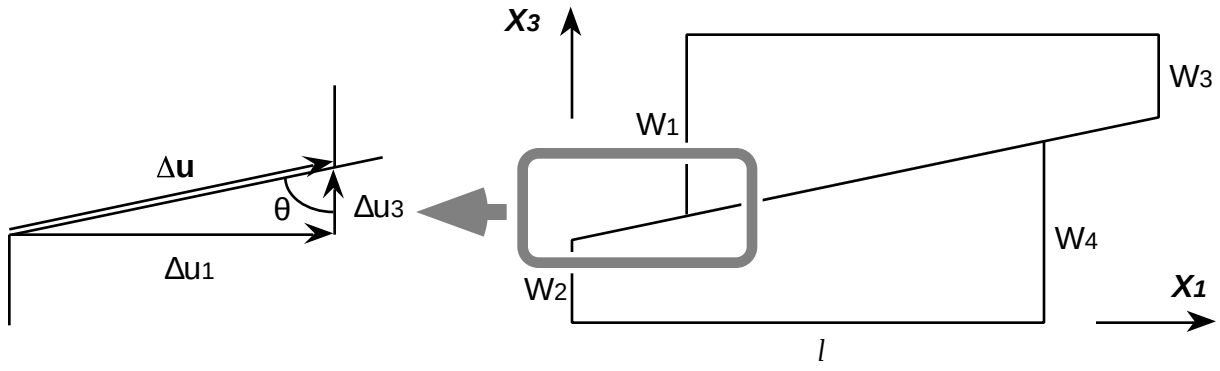

We see that the components of the displacement are:

$$\Delta u_1 = \Delta \mathbf{u} \sin\theta \qquad \text{and} \qquad \Delta u_3 = \Delta \mathbf{u} \cos\theta .$$

The length in the $\boldsymbol{X_3}$ direction is simple because the fault does not cut the top and bottom of the block (i.e. the sides of the block which are perpendicular to the $\boldsymbol{X_3}$ axis):

$$\Delta X_3 = W = (W_1 + W_2) = (W_3 + W_4)$$

The length in the $\boldsymbol{X_1}$ direction is more complicated because the fault cuts those sides (i.e. the sides of the block which are perpendicular to the $\boldsymbol{X_1}$ axis) and we will derive it indirectly below.

The extension parallel to the $\boldsymbol{X_3}$ axis, e_{33}, in terms of the slip and the geometric moment is:

$$e_{33} = \frac{\Delta u_3}{\Delta X_3} = \frac{\Delta \mathbf{u} \cos\theta}{W} = \frac{M_g \sin\theta \cos\theta}{V}$$

and the rotation toward $\boldsymbol{X_1}$ of a line originally parallel to $\boldsymbol{X_3}$, the off-diagonal component e_{13}, in terms of the slip and the geometric moment is:

$$e_{13} = \frac{\Delta u_1}{\Delta X_3} = \frac{\Delta \mathbf{u} \sin\theta}{W} = \frac{M_g \sin^2\theta}{V}.$$

To understand the problem of calculating ΔX_1, notice the effect of where the fault is located in the block on the displacement of the sides of the block:

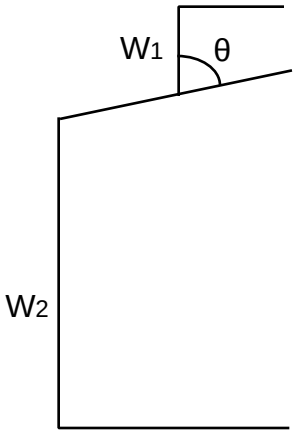

in this case, <u>almost none</u> of the left side has been displaced towards the right

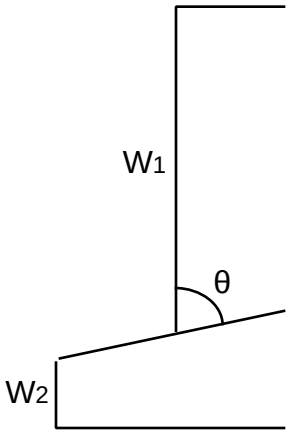

in this case, <u>most</u> of the left side has been displaced towards the right

In both cases, the average displacement of the left side of the block is a function of the ratio, W_1:W. Of course, just the opposite will be true for the right side of the block where the ratio will be W_3:W. In total, we get:

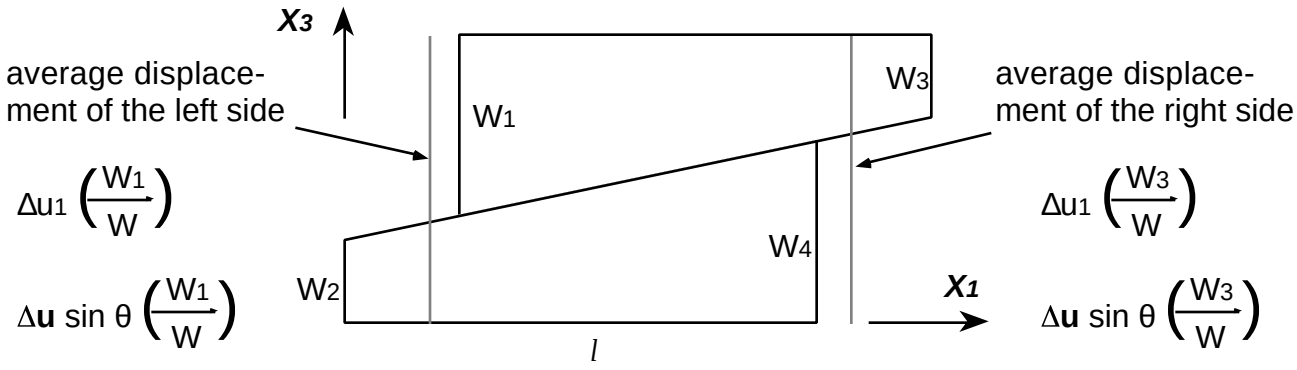

The extension in the direction of the X_1 axis, e_{11}, is:

$$e_{11} = \frac{\text{change in length}}{\text{initial length}} = \frac{\left(\frac{\Delta \mathbf{u} \sin\theta\, W_3}{W} - \frac{\Delta \mathbf{u} \sin\theta\, W_1}{W}\right)}{l}$$

or

$$e_{11} = \frac{\Delta \mathbf{u} \sin\theta\,(W_3 - W_1)}{W\,l} = \frac{\Delta u_1}{\left(\frac{W\,l}{(W_3 - W_1)}\right)} .$$

From some simple trigonometry, we get:

$$W_3 - W_1 = -L\cos\theta$$

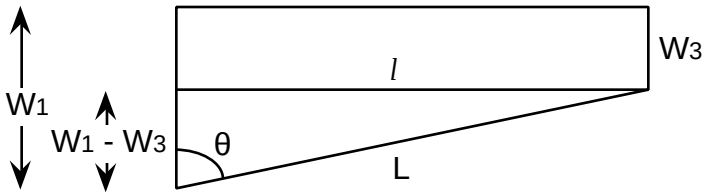

So, from this round about way, we see what ΔX_1 is:

$$\Delta X_1 = \frac{W\,l}{(W_3 - W_1)} = \frac{W\,l}{-L\cos\theta} .$$

Thus, e_{11}, in terms of the slip and in terms of the geometric moment, is:

$$e_{11} = \frac{-\Delta \mathbf{u}\, L \sin\theta\cos\theta}{W\,l} = \frac{-M_g \sin\theta\cos\theta}{V} .$$

The rotation toward $\boldsymbol{X_3}$ of a line originally parallel to $\boldsymbol{X_1}$, the off-diagonal component e_{31}, in terms of the slip and the geometric moment is:

$$e_{31} = \frac{\Delta u_3}{\Delta X_1} = \frac{\Delta \mathbf{u}\cos\theta}{\left(\frac{W\,l}{-L\cos\theta}\right)} = \frac{-\Delta \mathbf{u}\, L\cos^2\theta}{W\,l} = \frac{-M_g\cos^2\theta}{V}$$

So, in summary:

$$e_{ij} = \begin{bmatrix} -\sin\theta\cos\theta & \sin^2\theta \\ -\cos^2\theta & \sin\theta\cos\theta \end{bmatrix} \frac{M_g}{V}$$

Molnar (1983) calls this an asymmetric strain tensor but it really is the displacement gradient tensor, which is an asymmetric tensor. Note that, although we have done the derivation in two dimensions, the analysis

is easily generalizable to three dimensions.

2.3 -- UNIT SLIP AND NORMAL VECTORS

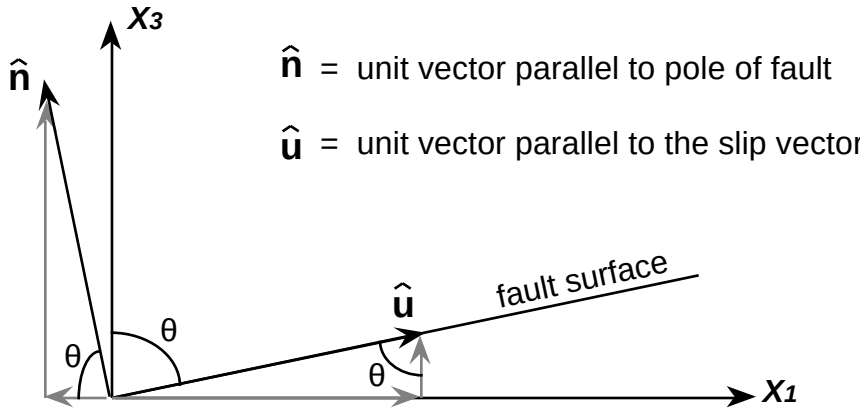

$\hat{\mathbf{n}}$ = unit vector parallel to pole of fault

From the above geometry, you can see that

$$\hat{\mathbf{u}} = \hat{i} \sin\theta + \hat{k} \cos\theta$$

$$\hat{\mathbf{n}} = -\hat{i} \cos\theta + \hat{k} \sin\theta$$

where $\hat{i}$ and $\hat{k}$ are unit vectors parallel to X_1 and X_3, respectively. Notice that, when we calculate the dyad product of $\hat{\mathbf{u}}$ and $\hat{\mathbf{n}}$ we get:

$$\hat{\mathbf{u}}\,\hat{\mathbf{n}} = \begin{bmatrix} \sin\theta \\ \cos\theta \end{bmatrix} \begin{bmatrix} -\cos\theta & \sin\theta \end{bmatrix} = \begin{bmatrix} -\sin\theta\cos\theta & \sin^2\theta \\ -\cos^2\theta & \sin\theta\cos\theta \end{bmatrix}$$

This is clearly the same matrix that we got before. So, we can define an **asymmetric moment tensor** as below:

$$M^{*}_{g_{ij}} = M_g\,\hat{\mathbf{u}}\,\hat{\mathbf{n}} = M_g\,u_i\,n_j$$

and the displacement gradient tensor, e_{ij} can be written:

$$e_{ij} = \frac{M^*_{g_{ij}}}{V}$$

To get the total displacement gradient tensor for the region, we can sum the moment tensors of all of the individual faults:

$$e_{ij\,(total)} = \frac{\sum^{n\ faults} M^*_{g_{ij}}}{V} .$$

2.4 -- PRACTICAL ASPECTS:

For each fault, the following measurements must be made:

1. The pole to the fault plane, $\hat{\mathbf{n}}$
2. The orientation of the slip vector, $\hat{\mathbf{u}}$ (which encompasses both the direction and the sense of slip)
3. The average slip, $\Delta\mathbf{u}$, and
4. The area of the fault surface.

For the first two, some convention must be adopted. The convention used does not matter as long as it is consistent throughout the area of study. Molnar and Deng (1984) defined $\hat{\mathbf{n}}$ so that it points into the eastern fault block and $\hat{\mathbf{u}}$ represents the movement of that block relative to the other. Alternatively, one can define so that it always points into the hangingwall block and shows the motion of that block.

The third and fourth items generally cannot be measured directly in the field and so must be calculated using some statistical method (Marrett and Allmendinger, in press). For example the average slip can be estimated using a fractal relation between fault gouge thickness and displacement. Alternatively, fault trace length may display a predictable relation to displacement (e.g. Walsh and Watterson, 1988). The basic idea is to determine some reasonable weighting factor which encompasses both the surface area and the average slip. This weighting factor should be determined in the region of interest and it should be selected so as to give a conservative estimate of the displacement (Marrett and Allmendinger, in press). These factors are discussed in the following section on 4. Practical Application.

Once the moment tensors are summed, there are two possible avenues. If you are interested just in the orientations of the principal axes, you can deal with the summed moment tensor directly. If you need magnitudes, then you must determine the volume of the region you are interested in (because the volume is a scalar, it affects the absolute magnitude (eigenvalues) but not the orientations (eigenvectors) of the principal axes).

Either way, the resulting asymmetric tensor can be divided into symmetric and antisymmetric components. The first gives the magnitudes and orientations of the principal axes and the second gives the orientation and magnitude of the rotation axis for the deformation:

$$e_{ij} = \varepsilon_{ij} + \omega_{ij} = \frac{e_{ij} + e_{ji}}{2} + \frac{e_{ij} - e_{ji}}{2}$$

The magnitudes and orientations of the principal axes of the symmetric part, ε_{ij}, can be calculated by determining the eigenvalues and eigenvectors for that matrix. The antisymmetric part, ω_{ij}, is what is known as an axial vector. To get the cartesian coordinates, R_i, of that vector:

$$R_i = - b_{ijk}\, \omega_{jk} / 2 .$$

b_{ijk} is a permutation symbol which is equal to +1 if the suffixes are cyclic, -1 if the suffixes are acyclic, and 0 if any two suffixes are repeated. The three components of **R**, which give the orientation of the rotation axis, are:

$$R_1 = - (\omega_{23} - \omega_{32}) / 2, \qquad R_2 = - (-\omega_{13} + \omega_{31}) / 2, \qquad \text{and} \qquad R_3 = - (\omega_{12} - \omega_{21}) / 2$$

The amount of rotation in *radians* is just the length of the vector, **R**:

$$||\mathbf{R}|| = \sqrt{R_1^2 + R_2^2 + R_3^2}$$

2.5 -- ASSUMPTIONS AND LIMITATIONS:

1. Infinitesimal strain: The dimensions of the region of interest must be large compared to the slip on the fault. Otherwise, the small angle assumptions etc. that enabled us to calculate the displacement gradient tensor no longer hold.

2. Fault must cut the boundaries of the region: This is primarily important to get rotation

out of the analysis. If the fault does not cut the boundary of the region, then the region itself cannot rotate (i.e. there must be some complementary rotation in the opposite sense elsewhere in the region to cancel out the rotation on the fault). In this case, we are left with a pure shear analysis like that by Kostrov (1974) (see below).

3. All of the assumptions and limitations that go into the practical inability to determine fault surface area and average slip directly…

2.6 -- KOSTROVS SYMMETRIC MOMENT TENSOR:

Kostrov (1974) determined a symmetric moment tensor:

$$M_{g\,ij} = M_g\left(\hat{\mathbf{u}}\,\hat{\mathbf{n}} + \hat{\mathbf{n}}\,\hat{\mathbf{u}}\right) = M_g\left(\hat{u}_i\,\hat{n}_j + \hat{u}_j\,\hat{n}_i\right)$$

and suggested that the regional strain could be determined by summing the tensors related to the individual faults:

$$\varepsilon_{ij\,(\text{total})} = \frac{\sum^{\text{n faults}} M_{g\,ij}}{2\,V}$$

Note the similarity of this equation to that for Molnars asymmetric tensor (p. 17). Jackson and McKenzie (1988) argue persuasively that Kostrovs symmetric moment tensor is the only legitimate one for general use. The issue is much like the dilemma faced by a geologist investigating, say, a deformed oolite: if one sees only the final state it is impossible to tell if the reference frame or the strain axes have rotated. The two possibilities are illustrated in the diagram below for the case of faulting:

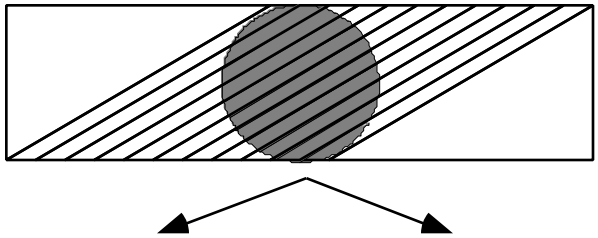

Simple shear rotation described by Molnar's Asymmetric Moment Tensor

Reference frame fixed to the faults
Faults do not rotate, region does rotate
Principal axes rotate in reference frame

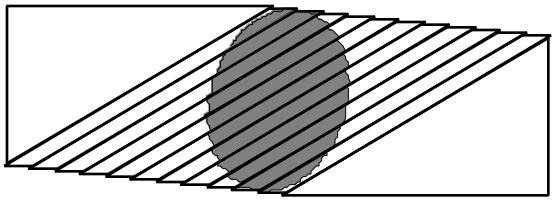

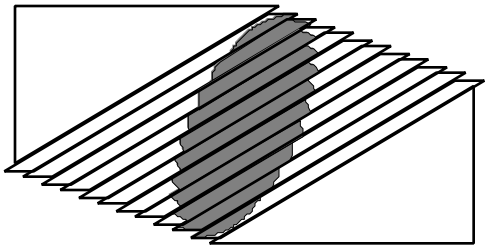

Rotation of region

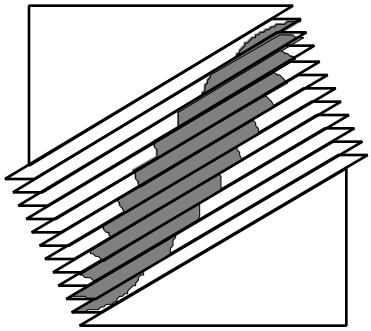

Pure shear rotation of faults not described by Molnar's Asymmetric Moment Tensor

Reference frame fixed to the region
Faults rotate, region does not rotate
Principal axes fixed in reference frame

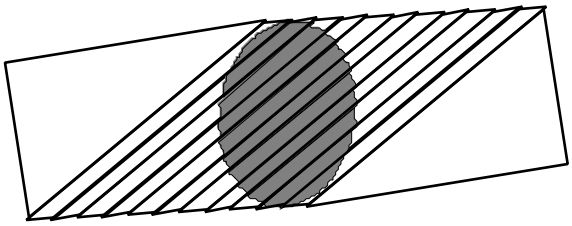

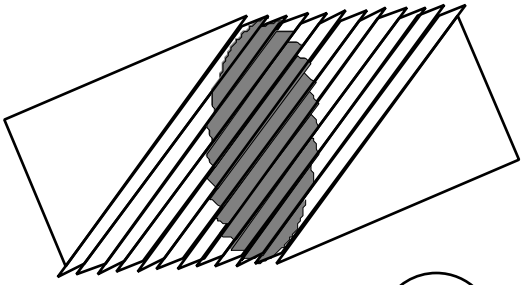

Rotation of faults

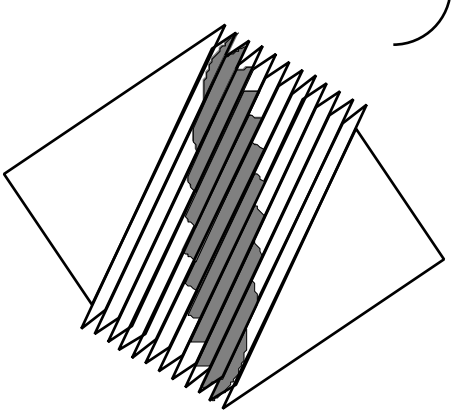

The exact relation between Molnars and Kostrovs tensor can be seen by decomposing the former into its symmetric and antisymmetric components:

$$M^*_{ij} = \frac{1}{2}(M^*_{ij} + M^*_{ji}) + \frac{1}{2}(M^*_{ij} - M^*_{ji}) .$$

In the above equation, the first set of terms on the right side is the symmetric part (ε_{ij} times the volume), and the second set is the antisymmetric part. Kostrovs tensor, written in terms of Molnars tensor, is

$$M_{ij} = (M^*_{ij} + M^*_{ji}) .$$

Thus, you can see that Kostrovs tensor, and the *symmetric part* of Molnars tensor differ only by a scalar factor of 2. In practical terms, this means that the orientations and the *relative* magnitudes of the principal axes of the moment tensor that one calculates will be the same for both. The only difference is that the absolute magnitudes of those axes will differ by a factor of 2. The factor of 2 disappears when you calculate strain; Kostrov divides his tensor by 2V (twice the volume) whereas Molnar divides by V.

One can argue that Molnars tensor potentially contains more information, particularly if field relations (or paleomagnetic data etc.) independently show that the faults do not rotate. Even if it is not known whether or not the faults rotate, the antisymmetric part of Molnars tensor describes the rotation of either the region or the faults themselves, although the sign of the rotation is opposite in the two cases. And, the symmetric strain tensor is the same in both cases.

2.7 -- FINAL REMARKS

Jackson and McKenzie (1988) point out that there is more information in the individual moment tensors than in the sum of the moment tensors across a deforming zone. This is true regardless of whether the symmetric or asymmetric moment tensor is used:

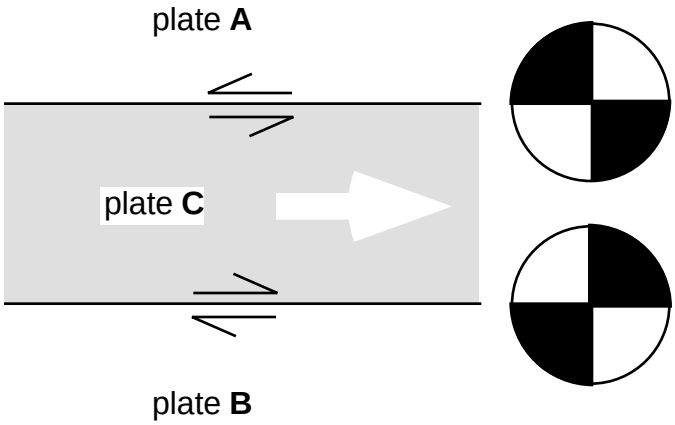

In this example (Jackson & McKenzies Figure 6), the sum of the moment tensors is zero: $\Sigma M_{ij} = 0$. This is because the sum only depends on the relative motion between plates **A** and **B**. Thus, one must be sure to split the region up into coherent structural domains.

3. GRAPHICAL ANALYSES OF FAULT SLIP DATA

by R. W. Allmendinger

A variety of kinematic and dynamic graphical methods of fault slip analysis have been proposed. Here we briefly review only two, the dynamic "P & T dihedra" method (Angelier and Mechler, 1977) and the kinematic "P" (shortening) and "T" (extension) axes. These two methods have proven to be the most robust; although they lack the precision of their more elegant numerical counterparts, they seldom differ substantially from numerical analyses of the same data. For other, more complicated graphical analyses, the reader is referred to the papers by Compton (1966), Arthaud (1969), and Aleksandrowski (1985).

3.1 -- P AND T AXES

Seismologists commonly use the letters "P" and "T" for to indicate axes which are located at 45° to the nodal planes of a fault plane solution and at 90° from the intersection of the nodal planes (known as the B-axis). These terms are illustrated in the equal area, lower hemisphere projections shown below:

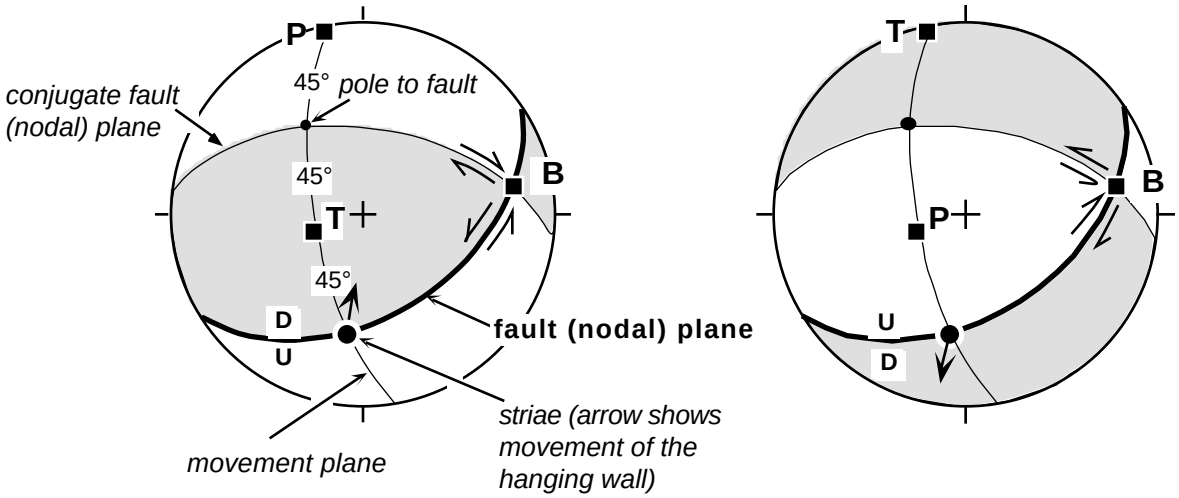

These letters, P and T, stand for the dynamic terms "pressure" and "tension," respectively, and some have equated these axes with the principal stress directions, $\sigma 1$ and σ_3. In fact, the axes would coincide

with the principal stress directions only if the fault plane and its conjugate were planes of maximum shear stress. This is unlikely, given both the relations of Coulomb fracture and the likelihood that much slip occurs on pre-existing fractures.

Despite their names, P and T axes are, in fact, infinitesimal principal shortening and extension directions which may, but do not have to, coincide with the principal stresses. Note that the calculation of P and T for a single fault involves the implicit assumption of plane strain, because there is no slip in the B direction. P and T axes will correspond to the principal axes of finite strain of a region only where faulting displays scale invariance and the strain is small or the strain path is coaxial (see the following discussion: "4. Practical Application").

Nonetheless, our tests have shown it to be a very good first approximation to the strain determined by more quantitative methods, and it is always the first analysis that we apply to the data. *Perhaps the greatest advantage of P and T axes are that, independent of their kinematic or dynamic significance, they are a simple, direct representation of fault geometry and the sense of slip. That is, one can view them as simply a compact alternative way of displaying the original <u>data</u> on which any further analysis is based. The results of most of the more sophisticated analyses commonly are difficult to relate to the original data; such is not the problem for P and T axes.*

P and T axes can be displayed as scatter plots or contoured for a more general overview (we prefer the method of Kamb, 1959). They can also be used as the basis for calculating an "unweighted" moment tensor summation which is realized by doing Bingham statistics in which the P and T axes are linked to one another. The following matrix K, composed of the sums of the products and the squares of the direction cosines of the individual P and T axes is calculated:

$$K = \begin{bmatrix} \sum(CN(P))^2 - (CN(T))^2 & \sum CN(P)*CE(P) - CN(T)*CE(T) & \sum CN(P)*CD(P) - CN(T)*CD(T) \\ \sum CE(P)*CN(P) - CE(T)*CN(T) & \sum(CE(P))^2 - (CE(T))^2 & \sum CE(P)*CD(P) - CE(T)*CD(T) \\ \sum CD(P)*CN(P) - CD(T)*CN(T) & \sum CD(P)*CE(P) - CD(T)*CE(T) & \sum(CD(P))^2 - (CD(T))^2 \end{bmatrix}$$

In the above matrix, CN(P) is the north direction cosine of the P-axis, CE(P) the east direction cosine, CD(P) the down direction cosine, etc. The eigenvalues and eigenvectors of K give the relative magnitudes and orientations of the kinematic axes.

One of the few potential artifacts that we have discovered using P and T dihedras occurs when then there

is a strong preferred orientation of fault planes but a wide variation in slip directions. The preferred orientations places a strong constraint on the possible position of P and T (basically at 45° to the pole to the average fault plane). It is not clear, however, that dynamic analyses are any better in this case.

3.2 -- THE P & T DIHEDRA

MacKenzie (1969) has pointed out, however, that particularly in areas with pre-existing fractures (which is virtually everywhere in the continents) there may be important differences between the principal stresses and P & T. In fact, the greatest principal stress may occur virtually anywhere within the P-quadrant and the least principal stress likewise anywhere within the T-quadrant. The P & T dihedra method proposed by Angelier and Mechler (1977) takes advantage of this by assuming that, in a population of faults, the geographic orientation that falls in the greatest number of P-quadrants is most likely to coincide with the orientation of σ_1. The diagram, below, shows the P & T dihedra analysis for three faults:

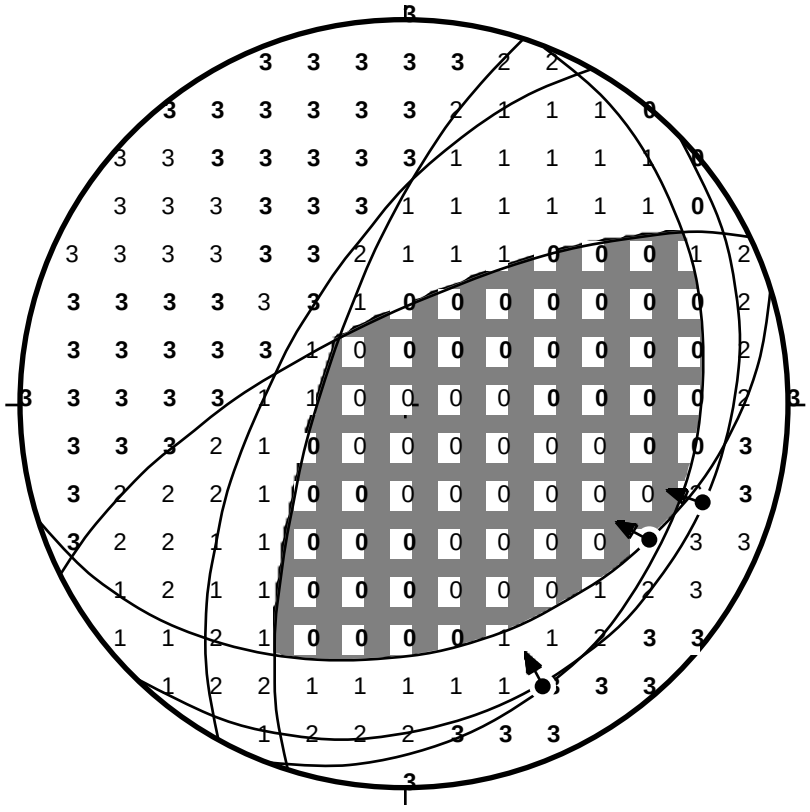

In the diagram, the faults are the great circles with the arrow-dot indicating the striae. The conjugate for each fault plane is also shown. The number at each grid point shows the number of individual P-quadrants

that coincide with the node. The region which is within the T-quadrants of all three faults has been shaded in gray. The bold face zeros and threes indicate the best solutions obtained using Lisle's (1987) AB-dihedra constraint. Lisle showed that the resolution of the P & T dihedra method can be improved by considering how the stress ratio, R, affects the analysis. The movement plane and the conjugate plane divide the sphere up into quadrants which Lisle labeled "A" and "B" (see figure below). If one principal stress lies in the region of intersection of the appropriate kinematic quadrant (i.e. either the P or the T quadrant) and the A quadrant then the other principal stress must lie in the B quadrant. In qualitative terms, this means that the $\sigma 3$ axis must lie on the same side of the movement plane as the $\sigma 1$ axis.

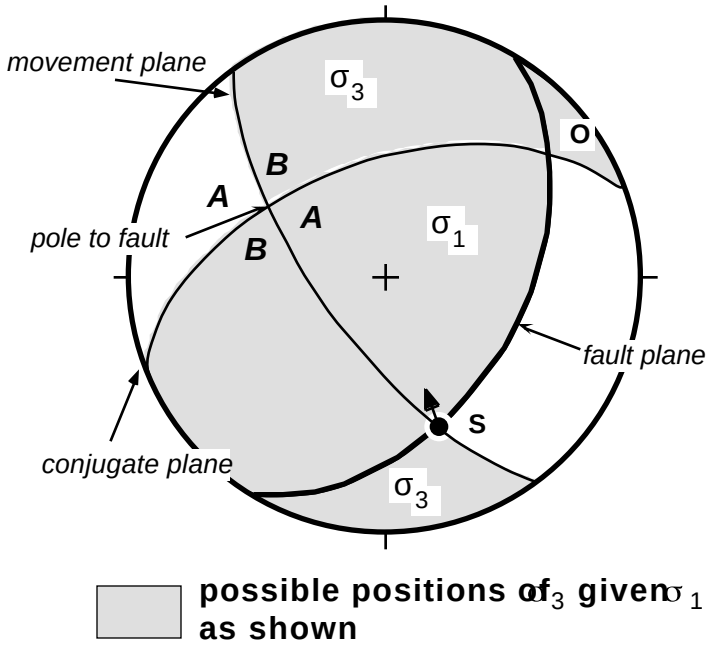

4. PRACTICAL APPLICATION OF FAULT SLIP METHODS

by R. A. Marrett & R. W. Allmendinger

4.1 -- FIELD MEASUREMENTS

The fault-slip datum should be measured at a relatively planar part of the fault which is at least subparallel to the megascopic orientation of the fault. Collection of field data for fault-slip analysis ideally would include measurement of several parameters for each of the faults studied:

- fault plane orientation,
- slip direction,
- sense-of-slip,
- local bedding orientation,
- average displacement, and
- fault surface area.

The first three are all that is required for the dynamic analysis techniques and for graphical kinematic methods, and usually those are all that are measured. To get considerably more out of the data however, the final three should also be measured or estimated. It is commonly impossible to reliably measure average displacement and fault surface area in the field due to inadequate exposure and our inability to see through rocks. In lieu of these parameters, *fault gouge thickness* and/or *fault width* can be used to estimate average displacement and fault surface area, and hence the magnitude of fault-slip deformation. Much of the discussion below applies more directly to kinematic analysis because it is more amenable to specific tests of validity.

4.1.1 --Shear Direction and Sense

The slip direction of a fault is usually determined from slickensides developed in the fault zone (Hancock & Barka 1987; Means 1987). Generally, a fault exposure must be excavated in several places in order to ensure that representative slickensides are chosen for measurement. Slickensides commonly vary locally in orientation by 10-20°. Distinct sets of slickensides, which differ by greater angles, may indicate fault

reactivation. Slip direction can also be determined from offset clasts and from offset piercing points defined by intersecting planar markers.

Fault scarps, stratigraphic relations, drag folding, vein-bearing fault steps, and offset clasts, veins and faults are the simplest and most reliable indicators. Fault plane surface indicators of sense-of-slip include tails and scratches produced by asperity ploughing (Means 1987), slickolite spikes (Arthaud & Mattauer 1972), and crescentic marks formed by the intersection of the fault plane with secondary fractures (Petit 1987). Many secondary fractures are useful sense-of-slip indicators, such as R, R', P, and T fractures (Petit 1987), bridge structures (Gamond 1987), and foliation in clay fault gouge (Chester & Logan 1987). However, their formation depends on the mechanical properties of the fractured rock and the physical conditions of deformation, so they can be ambiguous. Nevertheless, careful study of secondary fractures at faults of independently known sense-of-slip can identify criteria useful for observing other faults that formed under similar conditions in the same rock. Each fault should be carefully inspected for as many indicators as possible because interpretation of these subtle features can be difficult and contradictory indicators are commonly the only field evidence for a reactivated fault. It is also useful to develop a confidence scale, similar in concept to that used by seismologists to rank the quality of earthquake locations, to give one specific reason to retain or reject specific data.

Pages 29-31 show many of the possible sense-of-shear indicators for brittle faults.

Orientations of Common Fault-Related Features

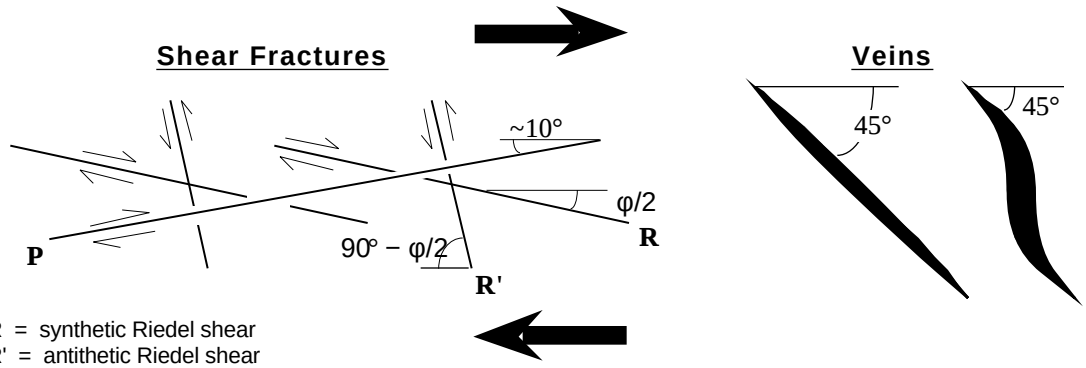

R = synthetic Riedel shear
R' = antithetic Riedel shear
P = P-shear; φ = angle of internal friction

Same sense of shear applies to all following diag

Riedel Shears

These features are well described in the classic papers by Tchalenko (1970), Wilcox et al. (1973), etc. The discussion below follows Petit (1987). It is uncommon to find unambiguous indicators of movement on the R or R' surfaces and one commonly interprets them based on striation and angle alone In my experience, R shears can be misleading and one should take particular care in using them without redundant indicators or collaborative indicators of a different type.

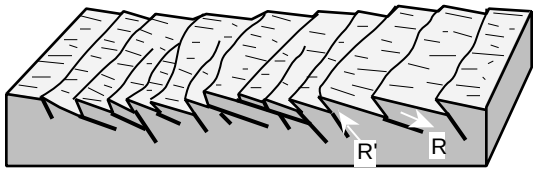

"RO"-Type (top): The fault surface is totally composed of R and R' surfaces. There are no P surfaces or an average surface of the fault plane. Fault surface has a serrated profile. Not very common.

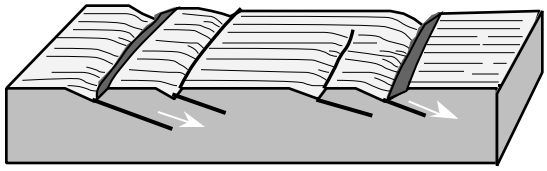

"RM"-Type (middle): The main fault surface is completely striated. R shears dip gently (5-15°) into the wall rock; R' shears are much less common. The tip at the intersection of R and the main fault plane commonly breaks off, leaving an unstriated step.

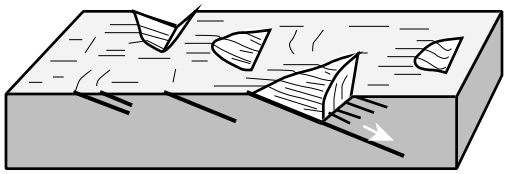

Lunate fractures (bottom): P shears commonly have concave curvature toward the fault plane, resulting in "half moon" shaped cavities or depressions in the fault surface.

diagrams modified after Petit (1987)

[sense of shear is top (missing) block to the right in all the diagrams on this page]

Striated P-Surfaces

These features were first described by Petit (1987). The fault plane is only partially striated, and the striations only appear on the up-flow sides of asperities.

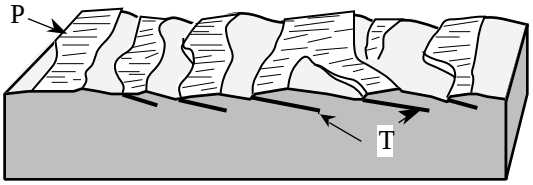

"PT"-Type (top & middle) planar, *non-striated* surfaces dip gently into the wall rock. Petit (1987) calls these "T" surfaces because of lack of evidence for shear, but they commonly form at angles more appropriate for R shears. Striated P surfaces face the direction in which that block moved. Steep steps developed locally at intersection between P and T. P surfaces may be relatively closely spaced (top) or much farther apart (middle).

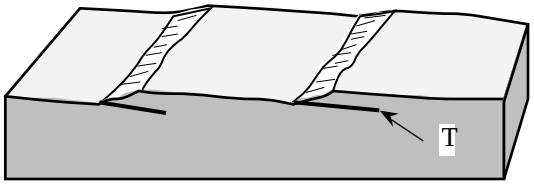

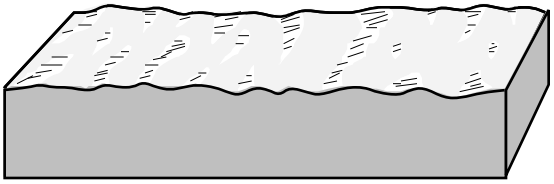

"PO"-Type (bottom) T surfaces are missing entirely. Striated P surfaces face in direction of movement of the block in which they occur. Lee side of asperities are unstriated.

diagrams modified after Petit (1987)

Unstriated Fractures ("T fractures")

Although "T" refers to "tension" it is a mistake to consider these as tensile fractures. They commonly dip in the direction of movement of the upper (missing) block and may be filled with veins or unfilled.

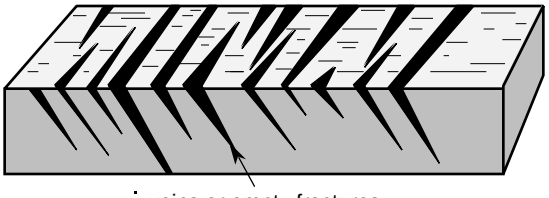

"Tensile Fractures" (top) If truely tensile in origin and formed during the faulting event, these should initiate at 45° to the fault plane and then rotate to higher angles with wall rock deformation. Many naturally occuring examples are found with angles between 30° and 90°. They are referred to as "comb fractures" by Hancock and Barka (1987).

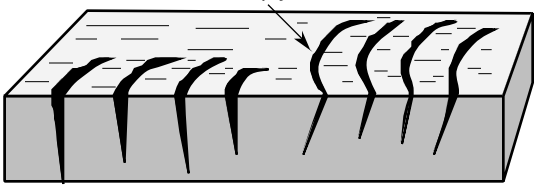

Crescent Marks (bottom) Commonly concave in the direction of movement of the upper (missing) block. They virtually always occur in sets and are usually oriented at a high angle to the fault surface. They are equivalent the "crescentic fractures" formed at the base of glaciers.

diagrams modified after Petit (1987)

[sense of shear is top (missing) block to the right in all the diagrams on this page]

"S-C" Fabrics

Although commonly associated with ductile shear zones, features kinematically identical to S-C fabrics also occur in brittle fault zones. There are two types: (1) those that form in clayey gouge in clastic rocks and (2) those that form in carbonates. They have not been described extensively in the literature. This is somewhat odd because I have found them one of the most useful, reliable, and prevalent indicators.

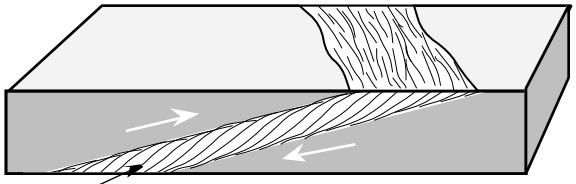

Clayey Gouge fabric (top): Documented by Chester and Logan (1987) and mentioned by Petit (1987). Fabric in the gouge has a sigmoidal shape very similar to S-surfaces in type-1 mylonites. This implies that the maximum strain in the gouge and displacement in the shear zone is along the walls. Abberations along faults may commonly be related to local steps in the walls.

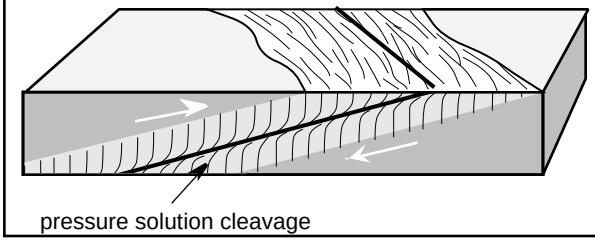

Carbonate fabric (top): This feature is particularly common in limestones. A pressure solution cleavage is localized in the walls of a fault zone. Because maximum strain and displacement is in the center of the zone rather than the edges, the curvature has a different aspect than the clayey gouge case. The fault surface, itself, commonly has slip-parallel calcite fibers.

Mineral Fibers & Tool Marks

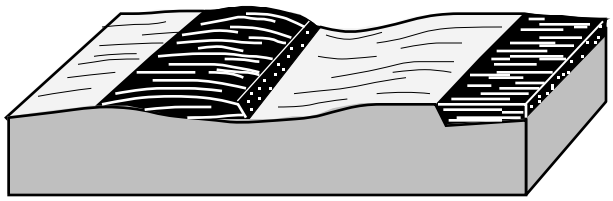

Mineral Fibers and Steps (top): When faulting occurs with fluids present along an undulatory fault surface or one with discrete steps, fiberous minerals grow from the lee side of the asperities where stress is lower and/or gaps open up. These are very common in carbonate rocks and less so in siliceous clastic rocks.

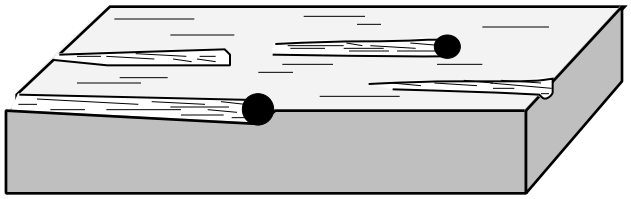

Tool Marks (bottom): This feature is most common in rocks which have clasts much harder that the matrix. During faulting, these clasts gouge the surface ("asperity ploughing" of Means [1987]), producinig trough shaped grooves. Although some attempt to interpret the grooves alone, to make a reliable interpretation, one must see the clast which produced the groove as well. Other- wise, it is impossible to tell if the deepest part of the groove is where the clast ended up or where it was plucked from.

[sense of shear is top (missing) block to the right in all the diagrams on this page]

4.2 -- ALTERNATIVE MEANS OF ESTIMATING THE MAGNITUDE OF FAULT-SLIP DEFORMATION

Although displacement and fault surface area can seldom be measured, several empirical relations make it possible to estimate the magnitude of deformation accommodated by a fault for which the average slip, D_{ave}, and fault surface area, A, are unknown. These estimates are based on field measurements of fault gouge thickness and/or maximum fault width (practically estimated by a field geologist as outcrop trace length).

4.2.1 -- Gouge Thickness

Models of fault growth (Sammis *et al*. 1987; Cox & Scholz 1988; Power *et al.* 1988) predict a linear increase of local fault gouge thickness (t) with local displacement (u) and data from cataclastic faults with displacements ranging from 10^{-2} m to 10^{4} m are consistent with this hypothesis (Scholz 1987; Hull 1988; this paper):

$$D = c_1 t$$

where c_1, an empirical constant, is a function of the magnitude of normal stress on the fault plane, the hardness of the rock, and the nature of the wear process (Scholz 1987). Empirical data for fault gouge vs. thickness shown on page 33 (be sure to read the notes at the bottom of that page) indicate that c_1 is about 60 to 70.

Fault gouge is noncohesive, multiply fractured material formed by brittle shear failure of rock (Sammis et al. 1987). Measurement of the thickness of fault gouge zones in the field presents several problems. Given the presence of asperities, t clearly varies from some maximum amount down to zero as a function of position along a fault. However, reliable estimates can be made by choosing a planar part of each fault and measuring the average fault gouge thickness in that area. The possible presence of unidentified horses (large coherent inclusions surrounded by highly deformed material) presents another problem, particularly for large faults. This can only be remedied in the field by observing large faults at many localities and integrating observations. Drag folding and attendant bedding-parallel slip pose an additional problem for large faults, because they can obscure the boundaries of the gouge zone by deforming adjacent wall rock.

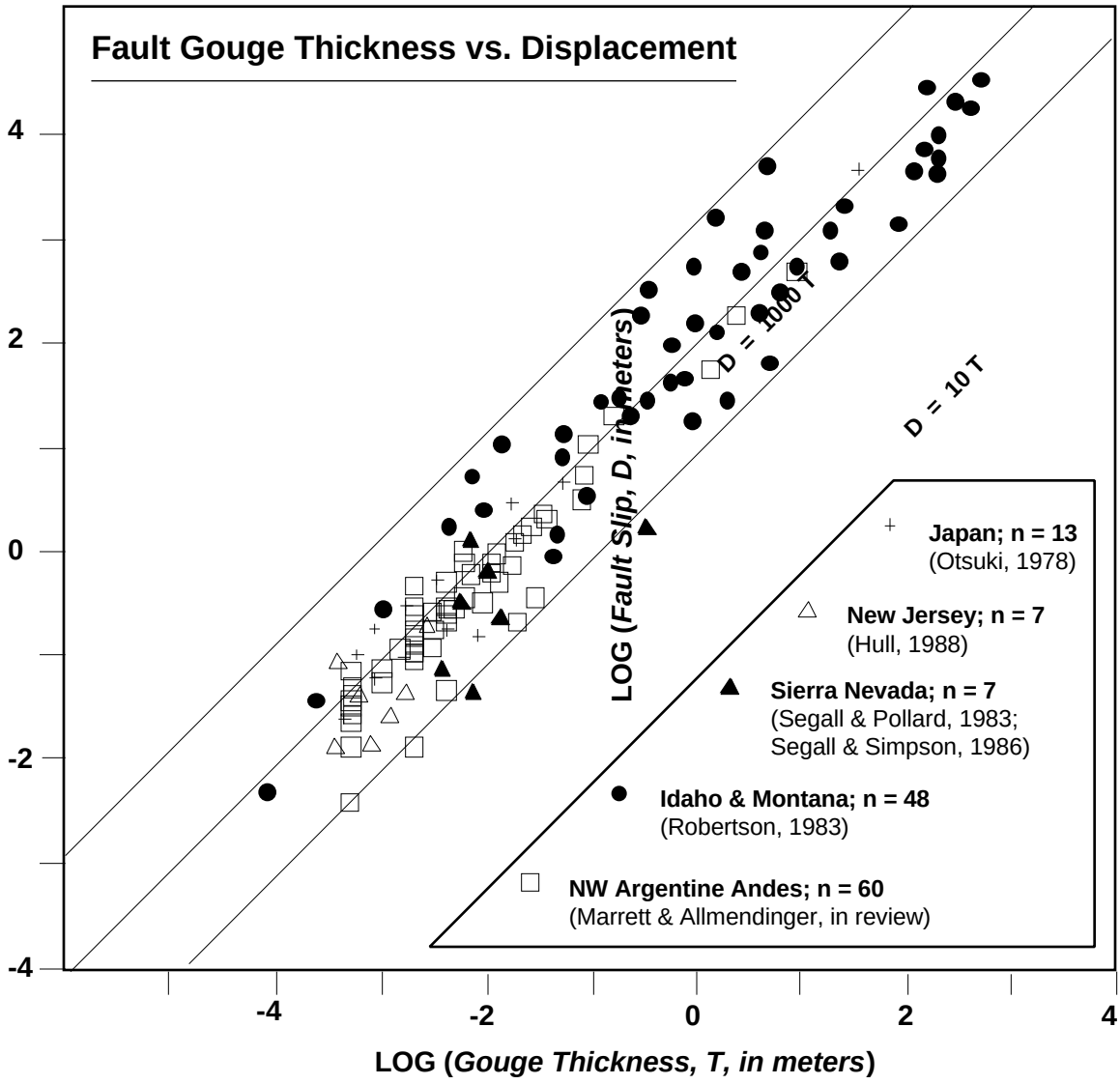

The gouge thickness versus displacement data plotted above come from a variety of rock types and tectonic environments. However, they are all from non-carbonate rocks in which the dominant mechanism is one of brittle cataclasis. As one can see, there is roughly a linear relationship (slope of 45° on a log-log plot) between gouge thickness and slip, which is in agreement with several fault growth models (Sammis et al., 1987; Scholz, 1987; Cox and Scholz, 1988; Power et al., 1988). Hull (1988) determined an average relationship of D = 63 * T, whereas Marrett and Allmendinger (in review) calculated that D = 70 * T. Although these numbers are remarkably close, considering the diverse tectonic environments, the most important thing to note in the graph above is that there are two orders of magnitude variation in gouge thickness vs. displacement. It is inappropriate to use the above relations to come up with a precise (although probably inaccurate) estimate of slip on any particular fault. The real value of these relations lies in their utility as weighting functions for quantitative kinematic analysis of faults via the moment tensor summation where strain depends on the square of the displacement. We suggest that one establishes their own D-T relationship for each area they work in rather than relying strictly on published results.

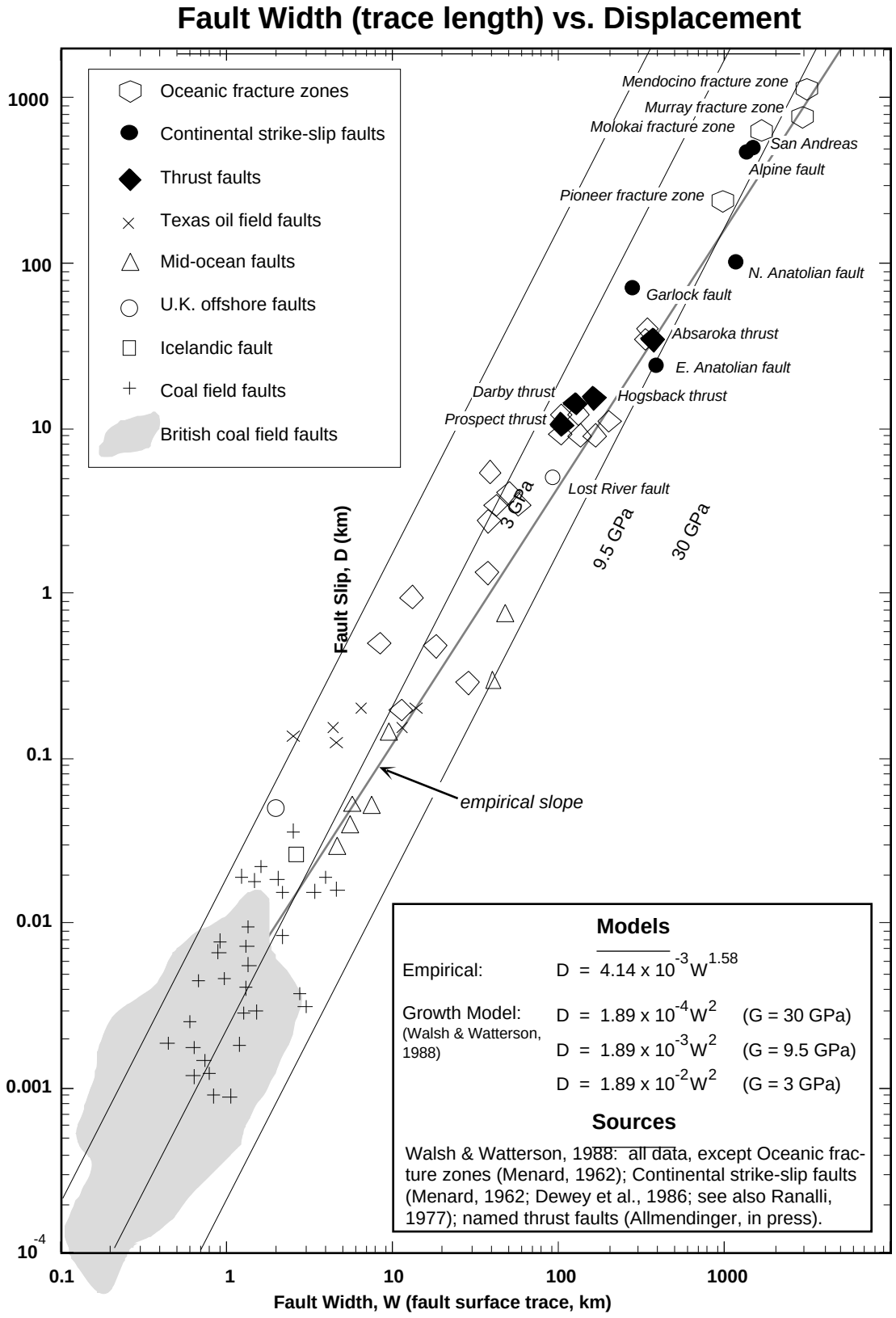
Fault Width (trace length) vs. Displacement
Oceanic fracture zones
Continental strike-slip faults
Thrust faults
Texas oil field faults
Mid-ocean faults
U.K. offshore faults
Icelandic fault
Coal field faults
British coal field faults
Mendocino fracture zone
Murray fracture zone
Molokai fracture zone
San Andreas
Alpine fault
Pioneer fracture zone
N. Anatolian fault
Garlock fault
Absaroka thrust
E. Anatolian fault
Darby thrust
Hogsback thrust
Prospect thrust
Lost River fault
3 GPa
9.5 GPa
30 GPa
empirical slope
Fault Slip, D (km)
Fault Width, W (fault surface trace, km)
1000
100
10
1
0.1
0.01
0.001
10^{-4}
0.1
1
10
100
1000
Models
Empirical: $D = 4.14 \times 10^{-3} W^{1.58}$
Growth Model: (Walsh & Watterson, 1988)
$D = 1.89 \times 10^{-4} W^{2}$ (G = 30 GPa)
$D = 1.89 \times 10^{-3} W^{2}$ (G = 9.5 GPa)
$D = 1.89 \times 10^{-2} W^{2}$ (G = 3 GPa)
Sources
Walsh & Watterson, 1988: all data, except Oceanic fracture zones (Menard, 1962); Continental strike-slip faults (Menard, 1962; Dewey et al., 1986; see also Ranalli, 1977); named thrust faults (Allmendinger, in press).

4.2.2 -- Fault Width (≈ Outcrop trace length)

Elliott (1976) suggested that fault surface trace length in plan view is linearly proportional to the maximum displacement (D_{max}) along the fault based on empirical grounds. Walsh & Watterson (1988) argue that maximum fault plane width (w) and maximum displacement have a parabolic relationship. They show that Elliott's data, along with new data, are empirically consistent with the following relationship:

$$D_{max} = \frac{c_2}{\mu^2} w^2,$$

where μ is the shear modulus and c_2 is a variable related to the stress drop of earthquakes averaging 2 x 10^{-4} GPa^2 m^{-1} for faults in a variety of rock types with displacements ranging from 10^0 m to 10^5 m (Walsh & Watterson 1988). Walsh and Watterson's data on width vs. displacement, along with data compiled by the authors, is shown on page 34.

Fault surface trace length usually is measured from air photos or maps rather than measured directly in the field. Because the complicated regions near fault tip lines are commonly small compared with the length of the fault, the uncertainty in trace length is not severe. More difficult is the assessment of the fault geometry at depth and in eroded rock, which is necessary to relate fault surface trace length (which is generally a chord in a simple elliptical fault model) to w. For many faults there is no alternative to assuming that they are the same, which if incorrect will always lead to an underestimation of w and therefore of D_{max}.

To use one of the empirical relationships above (preferably using empirical constants determined in the same study area in which it is to be used) in estimating the deformation magnitude of a fault, one must first relate D_{ave} with D and/or D_{max}, and also somehow evaluate A. The fractal nature of the faulting process (e.g. King 1983; Scholz & Aviles 1986; Turcotte 1986) suggests that the displacement functions of faults (u as a function of position on a fault surface) might be scale invariant, and detailed studies show that in a general way this is true (Muraoka & Kamata 1983; Higgs & Williams 1987; Walsh & Watterson 1987), although no data have been evaluated from faults with kilometers of displacement. This implies a simple linear relationship between D_{max} and D_{ave}:

$$D_{ave} = c_3 D_{max},$$

where c_3 is a constant which depends on the shape of the displacement function. For example, c_3 = 2/3 for an elliptical displacement function and c_3 = 1/3 for a triangular displacement function (see below). Faults tend to have displacement functions intermediate between elliptical and triangular (Muraoka & Kamata 1983; Higgs & Williams 1987; Walsh & Watterson 1987), so we will use c_3 = 1/2 below.

Characterizing the relationship between D and D_{ave} is less trivial. If one were to measure D at many points on a fault in a random way and average them, the result would probably be a good approximation of D_{ave}. In fact, if one were to measure D at only one randomly chosen point on a fault with an elliptical displacement function, the probability would be 89% of getting an answer within 50% of D_{ave}, as shown below for elliptical and triangular displacement functions.

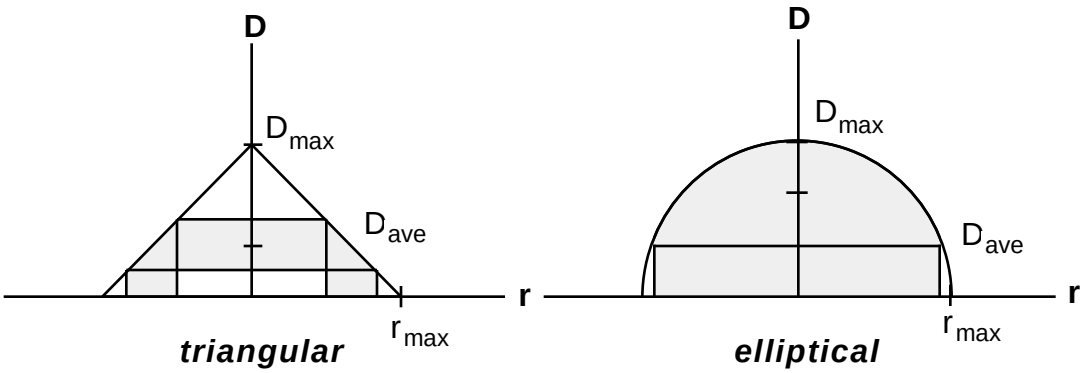

The cases in which the error is greater than 50% always lead to an underestimation of average displacement. Because the displacements observed for faults in typical arrays vary by several orders of magnitude, errors associated with assuming that D is statistically the same as D_{ave} will probably be relatively small. Thus we assume that $D_{ave} \approx D$.

Kanamori & Anderson (1975) successfully explained several empirically determined scaling laws of earthquakes using a model in which the surface area of slip is proportional to the square of average slip. Earthquakes and faults are not identical phenomena, because a large fault is the product of many earthquakes which have occurred in approximately the same place. The results of Walsh & Watterson (1988) imply that A is linearly proportional to D_{ave}, as seen by expressing A in terms of w:

$$A = \frac{\pi \, w^2}{4 \, e} = \frac{\pi \, \mu^2}{4 \, e \, c_2 \, c_3} \, D_{ave},$$

where e is the ellipticity of the fault surface. Although few data sets are available, data from both normal and thrust faults suggest that e varies between 2 and 3 (Walsh & Watterson 1987); we will use e = 2 below.

4.2.3 -- Geometric Moment as a Function of Gouge Thickness or Width

As described earlier, geometric moment (M_g) is a purely kinematic measure of deformation magnitude:

$$M_g = D_{ave} A$$

Substitution of previous equations into the above equation allows us to express M_g in terms of t and w. Equations 8 and 9 are the relations necessary for using the alternative means of estimating deformation magnitude:

$$M_g = \frac{\pi \mu^2 c_1^2}{4 e c_2 c_3} t^2,$$

$$M_g = \frac{\pi c_2 c_3}{4 e \mu^2} w^4.$$

These relationships are sufficient for *relative* weighting of the deformation magnitudes among observed faults whether or not the various constants are evaluated. However in the absence of determination of the constants, the relationships are insufficient for determining the absolute deformation magnitude for each fault. Using the values of c_1, c_2, c_3, and e cited above and $\mu = 12$ GPa (Walsh & Watterson 1988), approximate relationships for a hard sandstone are:

$$M_g \approx (3 \times 10^9 \text{ m}) \cdot t^2,$$

$$M_g \approx (3 \times 10^{-7} \text{ m}^{-1}) \cdot w^4.$$

4.3. TESTS OF SCALING, SAMPLING, AND ROTATION

Several of these tests are illustrated in the sample fault data set on pages 47-49, which follow this section.

4.3.1 -- Weighting Test

Weighting of fault-slip data is done in moment tensor summation with the geometric moment, as described above. In contrast, the graphical kinematic method assumes that fault kinematics are scale-invariant, such that faults of all magnitude ranges have similar kinematics and weighting is unnecessary. Thus faults with small magnitudes of deformation provide information as useful, for the purpose of determining the orientations of kinematic axes, as faults with large magnitudes of deformation. The graphical assumption can be qualitatively assessed by separating a data set into subgroups having geometric moments of different orders of magnitude and comparing their kinematics. Moment tensor summation for different subgroups should be compared with each other and with graphical analyses of the same subgroups. Fault kinematics appear to be scale invariant for many of the data sets that we have analyzed. This may represent a newly recognized fractal characteristic of the faulting process (e.g. King, 1983; Scholz & Aviles, 1986; Turcotte, 1986; Power *et al.,* 1987; Sammis *et al.,* 1987). It is important to emphasize, however, that scale invariance *must be established at each individual study area using the quantitative methods described, and not simply assumed* a priori.

4.3.2 -- Fold Test

Post-faulting reorientation of a fault-slip datum changes the orientations determined for the principal strain directions. The significance of differential rotation about horizontal axes can be characterized for a given data set by using a fold test similar to those used in paleomagnetic studies. The fold test consists of transforming the fault-slip measurements for each fault by the rotation necessary to return local bedding to horizontal, effectively unfolding the data. If the unfolding of a specific data set produces kinematics which are more coherent than the kinematics of the faults in their measured orientations, then folding probably post-dates faulting; if the unfolding of a specific data set produces kinematics which are less coherent than the kinematics of the faults in their measured orientations, then folding probably pre-dates faulting. Regional tilting, domino-style block rotation, and vertical axis rotation cannot be detected with this technique, but can be addressed using regional geologic and paleomagnetic data.

4.3.3 -- Sampling Test

Due to practical limitations inherent to field-based studies, only a small portion of the faults that exist in a given area are typically sampled. For the same reasons, a quantitative description of sampling is difficult to achieve and it is uncertain whether or not the observed faults are representative of the entire fault population. One way of proceeding is to conjecture that faults follow a power law number-magnitude relation, analogous to the frequency-magnitude relation earthquakes follow:

$$\log N = -B \cdot \log M_g + a. \tag{14}$$

Here N is the number of faults having M_g than a given value, B is analogous to the b-value of earthquakes determined seismologically (because faults and earthquakes are different phenomena, it is unnecessary that the two be identical), and a is log N having $M_g > 1\ m^3$. One way of determining this relation for a specific area is to determine the geometric moment for the largest two faults (M_g^1 and M_g^2). A line through the points (log M_g^1, log 1) and (log M_g^2, log 2) in a log-log plot characterizes both b and a, so that one can predict the number of faults that exist in any specific size range and quantify the percent of those faults actually observed. However, the use of just two faults cannot test the assumption of a power law number-magnitude relation. Alternatively, B might be determined by analyzing outcrops at which *all* faults (above a certain size threshold) can be identified and measured. Preferably, the size range of such outcrops would be as large as possible and the largest faults in the study area would also be analyzed. This would allow one to evaluate how well the fault population actually follows a power law number-magnitude relation.

Another measure with which sampling can be expressed is the portion of the total geometric moment sampled. The total geometric moment due to all faults can be written as a function of B and M_g^1:

$$\sum_{\text{faults}} M_g = M_g^1 \left[1 + \frac{1}{2^{1/B}} + \frac{1}{3^{1/B}} + \frac{1}{4^{1/B}} + \ldots \right].$$

This series converges only for B < 1; this is reasonable because B = 1 corresponds to the situation in which the sum of geometric moments of faults in each order of magnitude range are about the same (this is approximately the case for earthquakes). For example, faults with 1-10 mm displacements would, by virtue of their tremendous numbers, have as much geometric moment as faults with 1-10 km displacements. Were B = 1 for faults, construction of balanced cross-sections for the purpose of estimating strain magnitude would be a useless exercise.

In a test study area in NW Argentina which has excellent exposure, we are confident that the two biggest

faults were identified. Based on this assumption, B = 0.38 and a = 4.2, as shown in the figure below. The distance on the number-magnitude plot between the line and the points representing the observed faults (the shaded area) is a measure of the faults that should exist but which were not measured. For example, there should be 13 faults having $M_g > 10^8$ m^3 but only 5 were measured in the field, so about 38% of those faults were sampled.

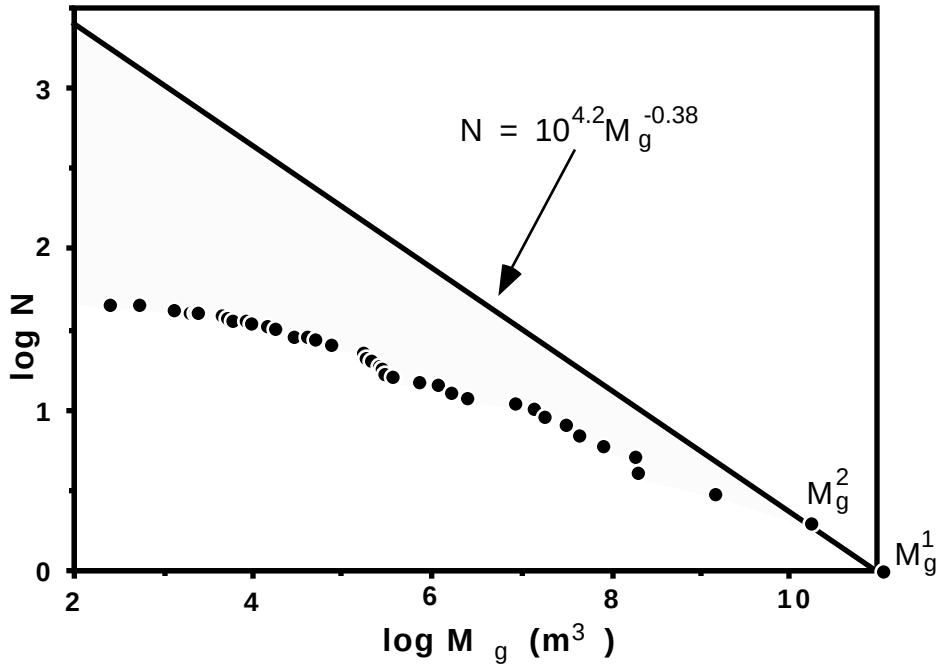

For B = 0.38,

$$\sum_{\text{faults}} M_g \quad 1.3 \quad M_g^1.$$

The largest fault alone accounts for nearly 80% of the total geometric moment. This suggests that the prospects of constructing a useful balanced cross-section of the study area are good. The faults measured in the field represent 93% of the total geometric moment, indicating that sampling is indeed representative of the entire fault population for this data set. Bear in mind, however, that this estimate is based on the untested assumption that the faults follow a power law number-magnitude relation.

4.3.4 -- Spatial Homogeneity Test

In principle, the kinematic methods do not assume that fault-slip kinematics are spatially homogeneous. However, group analysis of spatially heterogeneous data can obscure meaningful variation in the data by averaging statistically distinct subgroups. Testing for spatial homogeneity assures that such variation is

recognized. The degree of spatial homogeneity can be evaluated for a given data set by analyzing subgroups of faults from different domains and comparing their kinematics. The significance of kinematic heterogeneity is analyzed in the following section.

4.4 -- INTERPRETATION OF COMPLEX KINEMATIC PATTERNS

Kinematically heterogeneous faulting, represented by girdle or multi-modal patterns of shortening and/or extension axes, can be produced by several mechanisms: triaxial deformation, anisotropy reactivation, strain compatibility constraints, and/or multiple deformations. *Geologic evidence independent of fault-slip data provides the clearest indications of these mechanisms, however the absence of such evidence for a specific mechanism does not demonstrate its inactivity.* Graphical analysis of fault-slip data may allow more complete interpretation of kinematically complex faulting because each mechanism produces distinct patterns of poles-to-faults and slip directions which may be used to qualitatively assess the importance of each mechanism in a specific case.

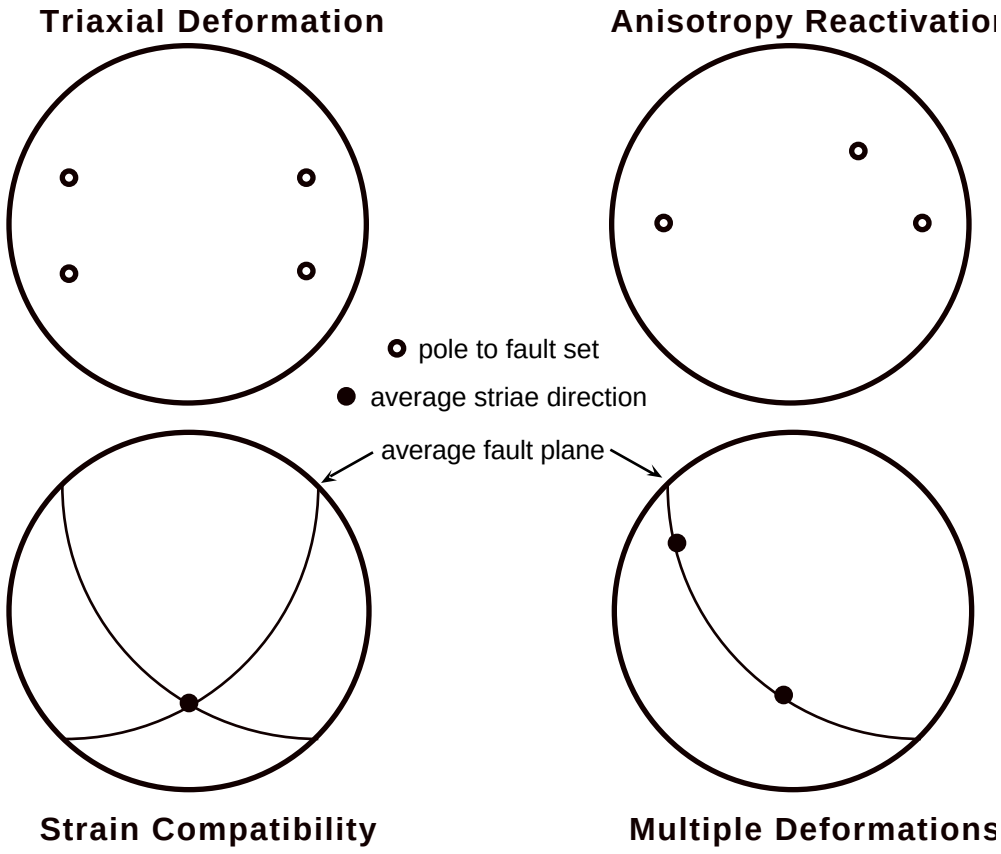

4.4.1 -- Triaxial Deformation

Reches (1983) showed that triaxial deformation produces three or four sets of faults arranged with orthorhombic symmetry and an equal number of distinct slip directions, also having orthorhombic symmetry. Such patterns have been observed in the field and in experiments (Donath 1962; Aydin & Reches 1982; Reches & Dieterich 1983). The degree to which the model of Reches (1983) fits a given data set provides a measure of how important the mechanism of triaxial deformation was in the development of the complex faulting observed. The presence of mutually cross-cutting fault sets supports the interpretation of triaxial deformation.

4.4.2 -- Anisotropy Reactivation

Deformations which are, in large part, kinematically homogeneous can nevertheless reactivate local, pre-existing anisotropies that are not ideally oriented for accommodating the overall deformation, thus producing locally heterogeneous kinematics. Anisotropies which exist only in units beneath those of interest can nevertheless control the kinematics in the overlying, previously unfractured rock. Because the orientation of pre-existing anisotropy is arbitrary with respect to the reactivating deformation, slip may be unsystematically oblique compared with slip on newly forming faults. Thus, reactivation of a basement anisotropy should produce a fault set which is not related to the other fault sets by a conjugate or orthorhombic symmetry, although the other fault sets may internally display such symmetry. The same is true of the slip directions. Independent data which support the interpretation of reactivation include a positive correlation between the orientations of a fault set and basement anisotropy and a positive correlation between spatial changes in fault-slip kinematics and changes in basement anisotropy orientations.

4.4.3 -- Strain Compatibility

Strain compatibility between two differently oriented faults or fault segments requires that they both must slip parallel to their line of intersection if no additional structures are to form. The greater the difference between the orientations of the faults or fault segments is, the greater the difference between their kinematics. This constraint will result in multiple sets of faults which have similar slip directions.

4.4.4 -- Multiple Deformations

Multiple deformations produce heterogeneous fault-slip kinematics when two deformations, each with internally coherent but distinct kinematics, affect the same rocks. Superposed deformations can produce a special kind of anisotropy reactivation in which previously active faults are reactivated, generating a second set of striae. Thus, individual faults may show evidence for slip in two or more different directions

and a single set of faults may have widely varying slip directions. The fault-slip kinematics of one deformation might also be incompatible with the kinematics of another deformation. Independent evidence for multiple deformations include systematic cross-cutting relations between fault sets and mutually exclusive chronologic constraints on fault sets.

5. EXAMPLE OF THE ANALYSIS OF A TYPICAL SMALL FAULT-SLIP DATA SET

The table below shows as typical small fault slip data set collected by Randy Marrett (Cornell) in northwestern Argentina. All of the faults were measured in Tertiary strata, with the exception of #6 which was measured in Quaternary sediments. This data set can lend itself nicely to exercises for students, or to follow through to test your own understanding. The calculation of P&T axes and the fold test can be done graphically, and those with programming knowledge can easily write a program to do the moment tensor summation (it's about 30-50 lines of code, without declarations or i/o). You will find the background for several of the analyses in Marrett and Allmendinger (in review).

LOCATION: Sierra de la Totora, Tucumán Province, Argentina
GEOLOGIST: R. A. Marrett
DATE: 30 May 1988

Fault #	Striations strike, dip§	trend, plunge	Sense of slip*	Slip (cm)	Gouge (cm)	Bedding strike, dip		Comments
1	358.	53. 104. 52.	T	?	0.3	352.0	54.0	
2	210.	40. 272. 37.	T	2.8	0.2	352.0	54.0	cuts #1
3	340.	30. 57. 29.	T	3.8	0.3	352.0	54.0	cuts #2
4	10.	55. 98. 55.	T	?	0.8	352.0	54.0	
5	3.	79. 158. 65.	L	?	2.8	352.0	54.0	
6	189.	80. 196. 35.	R	?	4.1	0.0	0.0	cuts Qal
7	201.	52. 284. 52.	T	2220.0	17.2	170.0	20.0	
8	204.	52. 336. 44.	T	?	210.0	213.0	48.0	
9	216.	70. 264. 64.	T	?	210.0	213.0	48.0	Same as 8
10	206.	61. 278. 60.	T	?	210.0	213.0	48.0	Same as 8

§ All dips are located clockwise from the given strike azimuth
* T = thrust, N = normal, R = right lateral, L = left lateral

The plots on the following pages show the determination and contouring of the P & T axes, the test to see if the faults formed before the folding, the results of the P&T dihedra calculation, the moment tensor sum for different size ranges, and plots of the kinematic axes as pseudo fault-plane solutions. All calculations were done with the program "Fault Kinematics," written by R. W. Allmendinger, R. A. Marrett, and T. Cladouhos. For the moment tensor sum, the gouge thicknesses and displacements were converted to scalar moments using equations 10 and 11 of Marrett and Allmendinger (in press).

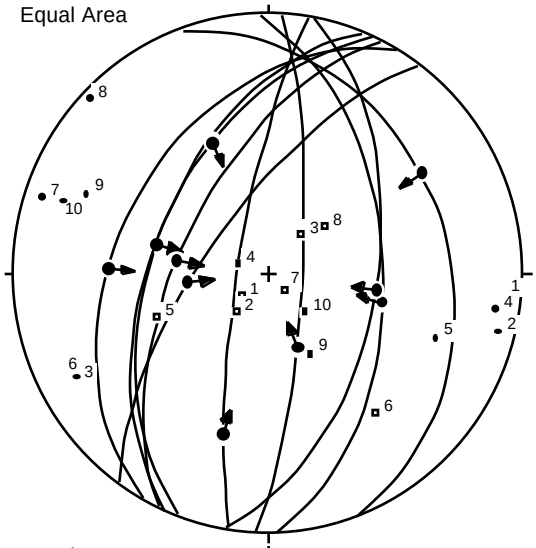

Example of Analysis of Fault Slip Data from the Sierra de la Totora, Tucumán Province, Argentina

1. Plot faults and striae and calculate "P" & "T" axes

Striae with arrow showing movement of hanging wall

Shortening ("P") axis (number is order in table)

Extension ("T") axis (number is order in table)

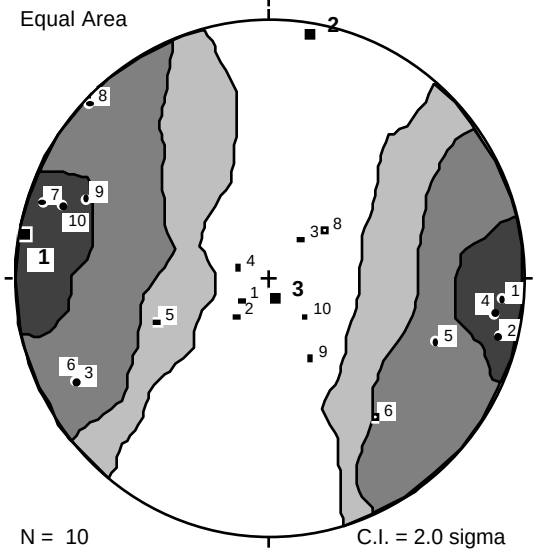

2. Contour P and T (not shown) axes and calculate unweighted moment tensor (linked Bingham) axes

Contouring of P-axes using Kamb (1959) method

Bingham axes shown with large numbers & black squares

Eigenvalue	Eigenvector trend	plunge
1. 0.3606	279.9°	3.1°
2. 0.189	10.2°	5.6°
3. -0.3795	161.2°	83.6°

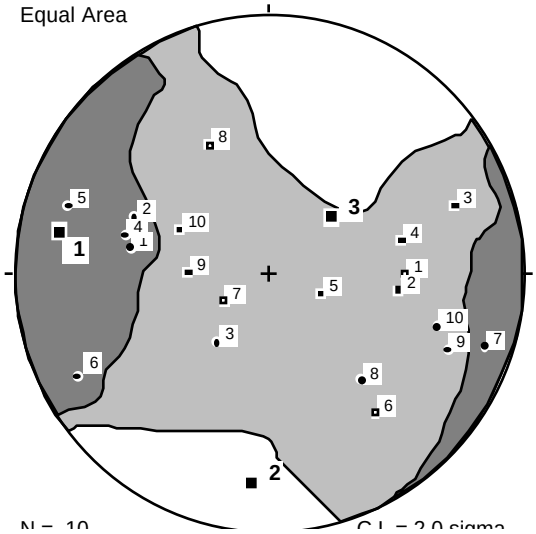

3. Fold test to see whether faulting before or after folding

Contouring of P-axes using Kamb (1959) method

Bingham axes shown with large numbers & black squares

Eigenvalue	Eigenvector trend	plunge
1. 0.1662	281.1°	17.6°
2. 0.0152	184.5°	19.8°
3. -0.1814	49.6°	63.0°

Both contouring and the Bingham analysis indicate faulting di not occur before folding.

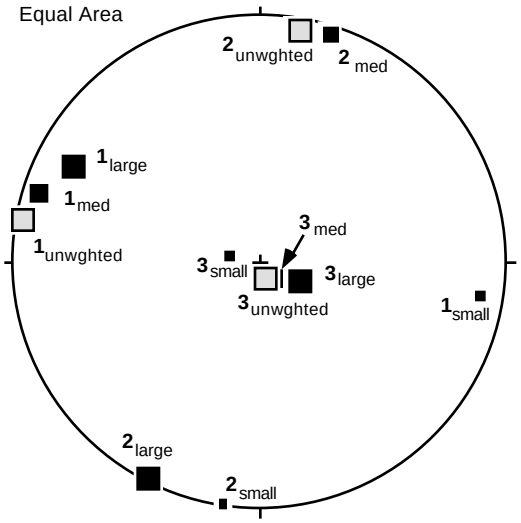

5. Moment tensor sum of all faults and sorted according to size ranges.

Small faults (#'s 1-4):	trend	plunge
1. 1.014 e 5	98.5°	9.6°
2. -1.298 e 2	188.5°	0.0°
3. -1.013 e 5	278.6°	80.4°
rotation axis =	8.5°	0.1°
magnitude = (-5.97 e 6)/volume		

Medium faults (#'s 4-6):	trend	plunge
1. 1.394 e 8	287.3°	7.0°
2. 4.615 e 5	17.8°	3.7°
3. -1.409 e 8	135.2°	82.0°
rotation axis =	18.2°	4.0°
magnitude = (8.00 e 9)/volume		

Largest fault (average of #'s 8-10):	trend	plunge
1. 5.692 e 9	297.2°	15.7°
2. -2.082 e 8	207.0°	0.7°
3. -5.531 e 9	114.5°	74.2°
rotation axis =	31.2°	0.6°
magnitude = (3.321 e 11)/volume		

All faults (n = 8):	trend	plunge
1. 5.828 e 9	296.9°	15.5°
2. -2.043 e 8	206.8°	0.5°
3. -5.666 e 9	114.9°	74.4°
rotation axis =	30.9°	0.7°
magnitude = (3.398 e 11)/volume		

The values of the principal axes of the moment tensor must be divided by volume to get strain. The rotation is a right hand rotation about the given axis. Note that a 1-2 order of magnitude change in displacement results in a 3 orders of magnitude change in the moment tensor (and in strain). This is the justification for using weighting parameters with variations of an order of magnitude, described previously. Notice also that the moments summed for all faults is nearly identical to the moment of just the largest fault.

4. P & T dihedra stress analysis (Angelier & Mechler, 1977), superimposed on contours of the "P" axes.

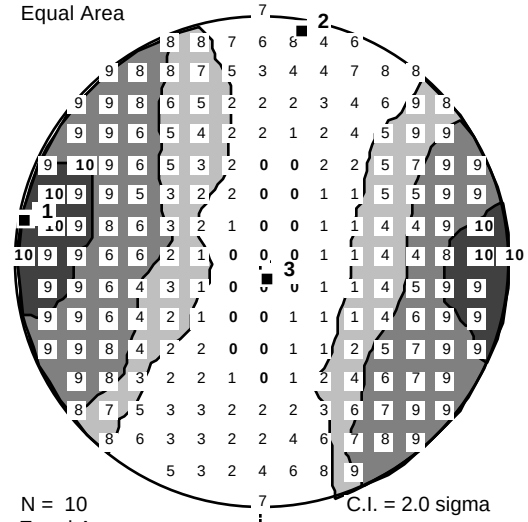

The numbers indicate the number of P quadrants that coincide with the grid node at which the number occurs. Note that good agreement, in this case, of the P dihedra with the contour of the P axes, but the poorer agreement of both with the moment tensor sum (#5, below).

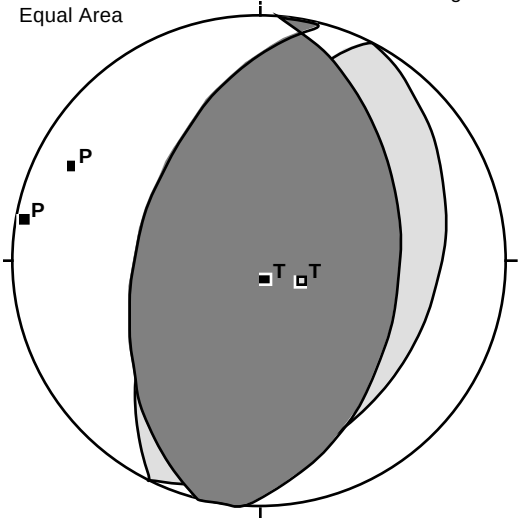

6. Plot of kinematic analyses of fault data as pseudo-fault plane solutions, using either moment tensor (light gray) or Bingham (dark gray) axes.

By convention, shaded quadrant is the "T" (extensional quadrant

6. FAULTS BIBLIOGRAPHY & REFERENCES CITED

Aleksandrowski, P., 1985, Graphical determination of principal stress directions for slickenside lineation populations: An attempt to modify Arthaud's method: Journal of Structural Geology, v. 7, p. 73-82.

Allmendinger, R. W., 1986, Tectonic development, southeastern border of the Puna Plateau, northwest Argentine Andes: Geological Society of America Bulletin, v. 97, p. 1070-1082.

Allmendinger, R. W., Marrett, R. A., and Grier, M. E., 1988, Extension, rotation, and strike-slip deformation in the Neogene-Quaternary Andes, 23°-33°S Latitude: Geological Society of America Abstracts with Programs, v. 20, p. in press.

Anderson, E. M., 1951, The dynamics of faulting and dyke formation with applications to Brittain: Edinburgh, Oliver & Boyd, 206 p.

Angelier, J., 1979, Determination of the mean principal directions of stresses for a given fault population: Tectonophysics, v. 56, p. T17-T26.

Angelier, J., 1984, Tectonic analysis of fault slip data sets: Journal of Geophysical Research, v. 89, p. 5835-5848.

Angelier, J., 1985, Extension and rifting: the Zeit region, Gulf of Suez: Journal of Structural Geology, v. 7, p. 605-611.

Angelier, J., 1989, From orientation to magnitudes in paleostress determinations using fault slip data: Journal of Structural Geology, v. 11, p. 37-50.

Angelier, J., Colletta, B., and Anderson, R. E., 1985, Neogene paleostress changes in the Basin and Range: A case study at Hoover Dam, Nevada-Arizona: Geological Society of America Bulletin, v. 96, p. 347-361.

Angelier, J., and Mechler, P., 1977, Sur une methode graphique de recherche des contraintes principales egalment utilisable en tectonique et en seismologie: La methode des diedres droits: Bulletin de Societie Geologique de France, v. 19, p. 1309-1318.

Angelier, J., Tarantola, A., Valette, B., and Manoussis, S., 1982, Inversion of field data in fault tectonics to obtain the regional stress. I, Single phase fault populations: A new method of computing the stress tensor: Geophys. J. R. Astron. Soc., v. 69, p. 607-621.

Armijo, R., Carey, E., and Cisternas, A., 1982, The inverse problem in microtectonics and the separation of tectonic phases: Tectonophysics, v. 82, p. 145-160.

Arthaud, F., 1969, Méthode de détermination graphique des directions de raccourcissement, d'allongement et intermédiare d'une population de failles: Bulletin Société Géologique de France, v. 11, p. 729-737.

Arthaud, R., and Mattauer, M., 1972, Sur l'origine tectonique de certains joints stylolitiques parallèles a la stratification; Leur relation avec une phase de distension (exemple du Languedoc): Bulletin Société Géologique de France, v. 14, p. 12-17.

Aydin, A., and Johnson, A. M., 1983, Analysis of faulting in porous sandstones: Journal of Structural

Geology, v. 5, p. 19-31.

Aydin, A., and Reches, Z., 1982, Number and orientation of fault sets in the field and in experiments: Geology, v. 10, p. 107-112.

Bartlett, W. L., Friedman, M., and Logan, J. M., 1981, Experimental folding and faulting of rocks under confining pressure, Part IX: Wrench faults in limestone layers: Tectonophysics, v. 79, p. 255-277.

Bergerat, F., 1987, Stress fields in the European platform at the time of Africa-Eurasia collision: Tectonics, v. 6, p. 99-132.

Blenkinsop, T. G., and Drury, M. R., 1988, Stress estimates and fault history from quartz microstructures: Journal of Structural Geology, v. 10, p. 673-684.

Bott, M. H. P., 1959, The mechanics of oblique slip faulting: Geological Magazine, v. 96, p. 109-117.

Brune, J.N., 1968, Seismic moment, seismicity, and rate of slip along major fault zones: Journal of Geophysical Research, v. 73, p. 777-784.

Bucknam, R. C., and Anderson, R. E., 1979, Estimation of fault-scarp ages from a scarp-height--slope-angle relationship: Geology, v. 7, p. 11-14.

Butler, P. R., Troxel, B. W., and Verosub, K. L., 1988, Late Cenozoic history and styles of deformation along the southern Death Valley fault zone, California: Geological Society of America Bulletin, v. 100, p. 402-410.

Byerlee, J., 1978, Friction of rocks: Pure and Applied Geophysics, v. 116, p. 615-626.

Cabrera, J., Sébrier, M., and Mercier, J. L., 1987, Active normal faulting in high plateaus of Central Andes: the Cuzco region (Peru): Annales Tectonicæ, v. 1, p. 116-138.

Carey, E., and Brunier, B., 1974, Analyse théorique et numérique d'un modèle mécanique élémentaire applequé à l'étude d'une population de failles: C. R. hebd. Séanc. Acad. Sci. Paris, D, v. 279, p. 891-894.

Célérier, B., 1988, How much does slip on a reactivated fault plane constrain the stress tensor?: Tectonics, v. 7, p. 1257-1278.

Chester, F. M., and Logan, J. M., 1987, Composite planar fabric of gouge from the Punchbowl Fault, California: Journal of Structural Geology, v. 9, p. 621-634.

Colman, S. M., and Watson, K., 1983, Ages estimated from a diffusion equation model for scarp degradation: Science, v. 221, p. 263-265.

Compton, R. R., 1966, Analysis of Pliocene-Pleistocene deformation and stresses in northern Santa Lucia Range, California: Geological Society of America Bulletin, v. 77, p. 1361-1380.

Cox, S. J. D., and Scholz, C. H., 1988, On the formation and growth of faults: an experimental study: Journal of Structural Geology, v. 10, p. 413-430.

Deng, Q., and Peizhen, Z., 1984, Research on the geometry of shear fracture zones: Journal of Geophysical Research, v. 89, p. 5699-5710.

Deng, Q., Sung, F., Zhu, S., Li, M., Wang, T., Zhang, W., Burchfiel, B. C., Molnar, P., and Zhang, P., 1984, Active faulting and tectonics of the Ningxia-Hui Autonomous Region, China: Journal

of Geophysical Research, v. 89, p. 4427-4445.

Donath, F., 1962, Analysis of Basin-Range structure, south-central Oregon: Geological Society of America Bulletin, v. 73, p. 1-16.

Ebinger, C. J., 1989, Geometric and kinematic development of border faults and accommodation zones, Kivu-Rusizi Rift, Africa: Tectonics, v. 8, p. 117-133.

Eisenstadt, G., and De Paor, D. G., 1987, Alternative model of thrust-fault propagation: Geology, v. 15, p. 630-633.

Elliott, D., 1976, The energy balance and deformation mechanisms of thrust sheets: Philosophical Transactions Royal Astronomical Society, v. A-283, p. 289-312.

Ellsworth, W. L., 1982, A general theory for determining state of stress in the earth from fault slip measurements: Terra Cognita, v. 2, p. 170-171.

Etchecopar, A., Vasseur, G., and Daignieres, M., 1981, An inverse problem in microtectonics for the determination of stress tensors from fault striation analysis: Journal of Structural Geology, v. 3, p. 51-65.

Faugère, E., Angelier, J., and Choukroune, P., 1986, Extension, décrochements et états de contrainte: la région de Las Vegas, Nevada (USA): Bulletin de la Société Géologique de France, v. 8(II), p. 871-877.

Frizzell, V. A., Jr., and Zoback, M. L., 1987, Stress orientation determined from fault slip data in Hampel Wash area, Nevada, and its relation to contemporary regional stress field: Tectonics, v. 6, p. 89-98.

Gamond, J. F., 1983, Displacement features associated with fault zones: A comparison between observed examples and experimental models: Journal of Structural Geology, v. 5, p. 33-45.

Gamond, J. F., 1987, Bridge structures as sense of displacement criteria in brittle fault zones: Journal of Structural Geology, v. 9, p. 609-620.

Gaviglio, P., 1986, Crack-seal mechanism in a limestone: A factor of deformation in strike-slip faulting: Tectonophysics, v. 131, p. 247-256.

Gephart, J. W., 1985, Principal stress directions and the ambiguity in fault plane identification from focal mechanisms: Bulletin of Seismological Society of America, v. 75, p. 621-625.

Gephart, J. W., 1988, On the use of stress inversion of fault-slip data to infer the frictional strength of rocks [abs.]: EOS (American Geophysical Union Transactions), v. 69, p. 1462.

Gephart, J. W., 1989, The Mohr sphere construction: Illustrating the relation between stress and fault-slip data [abs.]: Geological Society of America Abstracts with Programs, v. 21.

Gephart, J. W., in review, Stress and the direction of slip on fault planes: submitted to Tectonics.

Gephart, J. W., and Forsyth, D. W., 1984, An improved method for determining the regional stress tensor using earthquake focal mechanism data: Application to the San Fernando earthquake sequence: Journal of Geophysical Research, v. 89, p. 9305-9320.

Gibson, J. R., Walsh, J. J., and Watterson, J., 1989, Modelling of bed contours and cross-sections adjacent to planar normal faults: Journal of Structural Geology, v. 11, p. 317-328.

Grange, F., Hatzfeld, D., Cunningham, P., Molnar, P., Roecker, S. W., Suárez, G., Rodrígues, A, and Ocola, L., 1984, Tectonic implications of the microearthquake seismicity and fault plane solutions in southern Peru: Journal of Geophysical Research, v. 89, p. 6139-6152.

Gray, M. B., and Nickelsen, R. P., 1989, Pedogenic slickensides, indicators of strain and deformation processes in redbed sequences of the Appalachian foreland: Geology, v. 17, p. 72-75.

Hancock, P. L., and Barka, A. A., 1987, Kinematic indicators on active normal faults in western Turkey: Journal of Structural Geology, v. 9, p. 573-584.

Hancock, P. L., and Bevan, T. G., 1987, Brittle modes of foreland extension, in Coward, M. P., Dewey, J. F., and Hancock, P. L., eds., Continental extensional tectonics: Geological Society of London, Special Publication 28, p. 127-137.

Haneberg, W. C., 1988, Some possible effects of consolidation on growth fault geometry: Tectonophysics, v. 148, p. 309-316.

Hanks, T. C., Bucknam, R. C., Lajoie, K. R., and Wallace, R. E., 1984, Modifications of wave-cut and faulting-controlled landforms: Journal of Geophysical Research, v. 89, p. 5771-5790.

Hardcastle, K. C., 1989, Possible paleostress tensor configurations derived from fault-slip data in eastern Vermont and western New Hampshire: Tectonics, v. 8, p. 265-284.

Hempton, M. R., and Neher, K., 1986, Experimental fracture, strain and subsidence patterns over en échelon strike-slip faults: implications for the structural evolution of pull-apart basins: Journal of Structural Geology, v. 8, p. 597-605.

Higgs, W. G., and Williams, G. D., 1987, Displacement efficiency of faults and fractures: Journal of Structural Geology, v. 9, p. 371-374.

Huang, Q., 1988, Computer-based method to separate heterogeneous sets of fault-slip data into sub-sets: Journal of Structural Geology, v. 10, p. 297-299.

Hull, J., 1988, Thickness-displacement relationships for deformation zones: Journal of Structural Geology, v. 10, p. 431-435.

Jackson, J. A., and McKenzie, D. P., 1988, The relationship between plate motions and seismic moment tensors, and the rates of active deformation in the Mediterranean and Middle East: Geophysical Jouranl, v. 93, p. 45-73.

Jackson, J. A., and White, N. J., 1989, Normal faulting in the upper continental crust: observations from regions of active extension: Journal of Structural Geology, v. 11, p. 15-36.

Jaeger, J. C., and Cook, N. G. W., 1979, Fundamentals of Rock Mechanics, 3rd ed.: London, Chapman and Hall, 593 p.

Jones, L. M., 1988, Focal mechanisms and the state of stress on the San Andreas Fault in southern California: Journal of Geophysical Research, v. 93, p. 8869-8891.

Jones, T., and Nur, A., 1982, Seismic velocity and anisotropy in mylonites and the reflectivity of deep crustal faults: Geology, v. 10, p. 260-263.

Jones, T., and Nur, A., 1984, The nature of seismic reflections from deep crustal fault zones: Journal of Geophysical Research, v. 89, p. 3153-3171.

Jones, W. B., 1988, Listric growth faults in the Kenya Rift Valley: Journal of Structural Geology, v. 10,

p. 661-672.

Kamb, W. B., 1959, Ice petrofabric observations from Blue Glacier, Washington in relation to theory and experiment: Journal of Geophysical Research, v. 64, p. 1891-1909.

Kanamori, H., and Anderson, D., 1975, Theoretical basis of some empirical relations in seismology: Bulletin of the Seismological Society of America, v. 65, p. 1075-1095.

Kautz, S. A., and Sclater, J. G., 1988, Internal deformation in clay models of extension by block faulting: Tectonics, v. 7, p. 823-832.

King, G. C. P., 1983, The accommodation of large strains in the upper lithosphere of the Earth and other solids by self-similar fault systems: the geometrical origin of b-value: Pure and Applied Geophysics, v. 121, p. 761-815.

King, G. C. P., 1986, Speculations on the geometry of the initiation and termination processes of earthquake rupture and its relation to morphology and geologic structure: Pure and Applied Geophysics, v. 124, p. 567-585.

King, G. C. P., and Yielding, G., 1984, The evolution of a thrust fault system: processes of rupture initiation, propagation and termination in the 1980 El Asnam (Algeria) earthquake: Geophysical Journal of the Royal Astronomical Society, v. 77, p. 915-933.

Kleinspehn, K. L., Pershing, J., and Teyssier, C., 1989, Paleostress stratigraphy: A new technique for analyzing tectonic control on sedimentary-basin subsidence: Geology, v. 17, p. 253-256.

Kostrov, V. V., 1974, Seismic moment and energy of earthquakes, and seismic flow of rock: Izv. Acad. Sci. USSR Phys. Solid Earth, v. 1, p. 23-44.

Krantz, R. W., 1988, Multiple fault sets and three-dimensional strain: theory and application: Journal of Structural Geology, v. 10, p. 225-237.

Laurent, P., 1987, Shear-sense determination on striated faults from e twin lamellae in calcite: Journal of Structural Geology, v. 9, p. 591-595.

Lin, C.-H., Yeh, Y.-H., and Tsai, Y.-B., 1985, Determination of the regional principal stress directions in Taiwan from fault plane solutions: Bull. Inst. Earth Sciences, Academia Sinica, v. 5, p. 67-85.

Lisle, R. J., 1987, Principal stress orientations from faults: an additional constraint: Annales Tectonicæ, v. 1, p. 155-158.

Logan, J. M., and Rauenzahn, K. A., 1987, Frictional dependence of gouge mixtures of quartz and montmorillonite on velocity, composition and fabric: Tectonophysics, v. 144, p. 87-108.

Mandl, G., 1987, Tectonic deformation by rotating parallel faults: the "bookshelf" mechanism: Tectonophysics, v. 141, p. 277-316.

Mandl, G., 1987, Discontinuous fault zones: Journal of Structural Geology, v. 9, p. 105-110.

Mandl, G., 1988, Mechanics of tectonic faulting, models and basic concepts: Amsterdam, Elsevier, Developments in Structural Geology 1, 407 p.

Marrett, R. A., and Allmendinger, R. W., 1988, Graphical and numerical kinematic analysis of fault slip data [abs.]: Geological Society of America Abstracts with Programs, v. 20, p. in press.

Marrett, R. A., and Allmendinger, R. W., in press, Kinematic analysis of fault-slip data: Journal of Structural Geology, v. , p. .

McCaig, A. M., 1988, Deep fluid circulation in fault zones: Geology, v. 16, p. 867-870.

McKenzie, D. P., 1969, The relationship between fault plane solutions for earthquakes and the directions of the principal stresses: Bulletin of the Seismological Society of America, v. 59, p. 591-601.

Means, W. D., 1987, A newly recognized type of slickenside striation: Journal of Structural Geology, v. 9, p. 585-590.

Michael, A. J., 1984, Determination of stress from slip data: Faults and folds: Journal of Geophysical Research, v. 89, p. 11,517-11,526.

Michael, A. J., 1987, Use of focal mechanisms to determine stress: A control study: Journal of Geophysical Research, v. 92, p. 357-368.

Molnar, P., 1983, Average regional strain due to slip on numerous faults of different orientations: Journal of Geophysical Research, v. 88, p. 6430-6432.

Molnar, P., and Deng, Q., 1984, Faulting associated with large earthquakes and the average rate of deformation in central and eastern Asia: Journal of Geophysical Research, v. 89, p. 6203-6227.

Moore, D. E., Summers, R., and Byerlee, J. D., 1989, Sliding behavior and deformation textures of heated illite gouge: Journal of Structural Geology, v. 11, p. 329-342.

Mount, V. S., and Suppe, J., 1987, State of stress near the San Andreas fault: Implications for wrench tectonics: Geology, v. 15, p. 1143-1146.

Muraoka, H., and Kamata, H., 1983, Displacement distribution along minor fault traces: Journal of Structural Geology, v. 5, p. 483-495.

Naylor, M. A., Mandl, G., and Sijpesteijn, C. H. K., 1986, Fault geometries in basement-induced wrench faulting under differential initial stress states: Journal of Structural Geology, v. 8, p. 737-752.

Nicholson, C., Seeber, L., Williams, P., and Sykes, L. R., 1986, Seismic evidence for conjugate slip and block rotation within the San Andreas fault system, southern California: Tectonics, v. 6, p. 629-648.

Nye, J. F., 1985, Physical properties of crystals; their representation by tensors and matrices, 2nd ed.: Oxford, England, Oxford University Press, 329 p.

Obee, H. K., and White, S. H., 1986, Microstructural and fabric heterogeneities in fault rocks associated with a fundamental fault: Philosophical Transactions of the Royal Society of London, v. A-317, p. 99-109.

Oppenheimer, D. H., Reasenberg, P. A., and Simpson, R. W., 1988, Fault plane solutions for the 1984 Morgan Hill, California, earthquake sequence: Evidence for the state of stress on the Calaveras fault: Journal of Geophysical Research, v. 93, p. 9007-9026.

Parker, R. L., and McNutt, M. K., 1980, Statistics for the one norm misfit measure: Journal of Geophysical Research, v. 85, p. 4429-4430.

Parry, W. T., and Bruhn, R. L., 1987, Fluid inclusion evidence for minimum of 11 km vertical offset on

the Wasatch fault, Utah: Geology, v. 15, p. 67-70.

Petit, J. -P., 1987, Criteria for the sense of movement on fault surfaces in brittle rocks: Journal of Structural Geology, v. 9, p. 597-608.

Petit, J. -P., and Barquins, M., 1988, Can natural faults propagate under mode II conditions?: Tectonics, v. 7, p. 1243-1256.

Petit, J.-P., Proust, F., and Tapponnier, P., 1983, Critères de sens de mouvement sur les miroirs de failles en roches non calcaires: Bulletin de la Société Géologique de France, v. 7(XXV), p. 589-608.

Power, W. L., Tullis, T. E., Brown, S. R., Boitnott, G. N., and Scholz, C. H., 1987, Roughness of natural fault surfaces: Geophysical Research Letters, v. 14, p. 29-32.

Price, R. A., 1967, The tectonic significance of mesoscopic subfabrics in the Southern Rocky Mountains of Alberta and British Columbia: Canadian Journal Earth Sciences, v. 4, p. 39-70.

Reches, Z., 1983, Faulting of rocks in three-dimensional strain fields: II. Theoretical analysis: Tectonophysics, v. 95, p. 133-156.

Reches, Z., 1987, Determination of the tectonic stress tensor from slip along faults that obey the Coulomb yield condition: Tectonics, v. 6, p. 849-861.

Reches, Z., 1988, Evolution of fault patterns in clay experiments: Tectonophysics, v. 145, p. 129-140.

Reches, Z., and Dieterich, J., 1983, Faulting of rock in three-dimensional strain fields: I. Failure of rocks in polyaxial, servo-control experiments: Tectonophysics, v. 95, p. 111-132.

Robertson, E. C., 1982, Continuous formation of gouge and breccia during fault displacement, in Goodman, R. E., and Hulse, C., eds., Issues in rock mechanics: New York, American Institute of Mining Engineers, p. 397-404.

Robertson, E. C., 1983, Relationship of fault displacement to gouge and breccia thickness: American Institute of Mining Engineers Transactions, v. 274, p. 1426-1432.

Ron, H., Aydin, A., and Nur, A., 1986, Strike-slip faulting and block rotation in the Lake Mead fault system: Geology, v. 14, p. 1020-1023.

Sammis, C., King, G. C. P., and Biegel, R., 1987, Kinematics of gouge formation: Pure and Applied Geophysics, v. 125, p. 777-812.

Sassi, W., and Carey-Gailhardis, E., 1987, Interprétation mécanique du glissement sur les failles: introduction d'un critère de frottement: Annales Tectonicæ, v. 1, p. 139-154.

Scholz, C. H., 1987, Wear and gouge formation in brittle faulting: Geology, v. 15, p. 493-495.

Scholz, C. H., and Aviles, C. A., 1986, The fractal geometry of faults and faulting, in Das, S., Boatwright, J., and Scholz, C., eds., Earthquakes source mechanics: Washington, D. C., American Geophysical Union, Monograph 37, p. 147-156.

Schwartz, D. P., 1988, Paleoseismicity and neotectonics of the Cordillera Blanca fault zone, northern Peruvian Andes: Journal of Geophysical Research, v. 93, p. 4712-4730.

Schwartz, D. P., and Coppersmith, K. J., 1984, Fault behavior and characteristic earthquakes: Examples from the Wasatch and San Andreas fault zones: Journal of Geophysical Research, v. 89, p.

5681-5698.

Sébrier, M., Mercier, J. L., Macharé, J., Bonnot D., Cabrera, J., and Blanc, J. L., 1988, The state of stress in an overriding plate situated above a flat slab: The Andes of central Peru: Tectonics, v. 7, p. 895-928.

Sébrier, M., Mercier, J. L., Mégard, F., Laubacher, G., and Carey-Gailhardis, E., 1985, Quaternary normal and reverse faulting and the state of stress in the central Andes of south Peru: Tectonics, v. 4, p. 739-780.

Segall, P., and Pollard, D. D., 1980, Mechanics of discontinuous faults: Journal of Geophysical Research, v. 85, p. 4337-4350.

Segall, P., and Pollard, D. D., 1983, Joint formation in the granitic rock of the Sierra Nevada: Geological Society of America Bulletin, v. 94, p. 563-575.

Sibson, R. H., 1974, Frictional constraints on thrust, wrench and normal faults: Nature, v. 249, p. 542-544.

Sibson, R. H., 1977, Fault rocks and fault mechanisms: Journal of the Geological Society of London, v. 133, p. 191-213.

Sibson, R. H., 1982, Fault zone models, heat flow, and the depth distribution of earthquakes in the continental crust of the United States: Bulletin of the Seismological Society of America, v. 72, p. 151-163.

Sibson, R. H., 1983, Continental fault structure and the shallow earthquake source: Journal of the Geological Society of London, v. 140, p. 741-767.

Sibson, R. H., 1986, Brecciation processes in fault zones: Inferences from earthquake rupturing: Pure and Applied Geophysics, v. 124, p. 159-176.

Sibson, R. H., 1987, Earthquake rupturing as a mineralizing agent in hydrothermal systems: Geology, v. 15, p. 701-704.

Sibson, R. H., 1989, Earthquake faulting as a structural process: Journal of Structural Geology, v. 11, p. 1-14.

Suárez, G., Molnar, P., and Burchfiel, B. C., 1983, Seismicity, Fault plane solutions, depth of faulting, and active tectonics of the Andes of Peru, Ecuador, and southern Colombia: Journal of Geophysical Research, v. 88, p. 10403-10428.

Tchalenko, J. S., 1970, Similarities between shear zones of different magnitudes: Geological Society of America Bulletin, v. 81, p. 1625-1640.

Turcotte, D. L., 1986, A fractal model for crustal deformation: Tectonophysics, v. 132, p. 261-269.

Vasseur, G., Etchecopar, A., and Philip, H., 1983, State of stress inferred from multiple focal mechanisms: Annales Geophysicae, v. 1, p. 291-298.

Wallace, R. E., 1977, Profiles and ages of young fault scarps, north-central Nevada: Geological Society of America Bulletin, v. 88, p. 1267-1281.

Wallace, R. E., 1984, Patterns and timing of Late Quaternary faulting in the Great Basin Province and relation to some regional tectonic features: Journal of Geophysical Research, v. 89, p. 5763-5769.

Walsh, J. J., and Watterson, J., 1987, Distributions of cumulative displacement and seismic slip on a single normal fault surface: Journal of Structural Geology, v. 9, p. 1039-1046.

Walsh, J. J., and Watterson, J., 1988, Analysis of the relationship between displacements and dimensions of faults: Journal of Structural Geology, v. 10, p. 239-247.

Walsh, J. J., and Watterson, J., 1989, Displacement gradients on fault surfaces: Journal of Structural Geology, v. 11, p. 307-316.

White, S. H., Bretan, P. G., and Rutter, E. H., 1986, Fault-zone reactivation: kinematics and mechanisms: Philosophical Transactions of the Royal Society of London, v. A-317, p. 81-97.

Wilcox, R. E., Harding, T. P., and Seely, D. R., 1973, Basic wrench tectonics: American Association of Petroleum Geologists Bulletin, v. 57, p. 74-96.

Wojtal, S., 1986, Deformation within foreland thrust sheets by populations of minor faults: Journal of Structural Geology, v. 8, p. 341-360.

Woodcock, N. H., 1987, Kinematics of strike-slip faulting, Builth Inlier, Mid-Wales: Journal of Structural Geology, v. 9, p. 353-363.

Zoback, M. D., and Healy, J. H., 1984, Friction, faulting, and "in situ" stress: Annales Geophysicae, v. 2, p. 689-698.

Zoback, M. D., Zoback, M. L., Mount, V. S., Suppe, J., Eaton, J. P., Healy, J. H., Oppenheimer, D., Reasenberg, P., Jones, L., Raleigh, C. B., Wong, I. G., Scotti, O., and Wentworth, C., 1987, New evidence on the state of stress of the San Andreas fault system: Science, v. 238, p. 1105-1111.

Zoback, M. L., 1983, Structure and Cenozoic tectonism along the Wasatch fault zone, Utah, in Miller, D. M., Todd, V. R., and Howard, K. A., eds., Tectonic and stratigraphic studies in the Eastern Great Basin: Boulder, Colorado, Geological Society of America, Memoir 157, p. 3-28.